DESIGNS OF A PLANAR WAVEGUIDE SOLAR CONCENTRATOR

A Dissertation

by

YUXIAO LIU

Submitted to the Office of Graduate and Professional Studies of
Texas A&M University
in partial fulfillment of the requirements for the degree of

DOCTOR OF PHILOSOPHY

Chair of Committee,	Christi Madsen
Committee Members,	Ohannes Eknoyan
	Robert Nevels
	Alexey Belyanin
Head of Department,	Miroslav Begovic

December 2015

Major Subject: Electrical Engineering

ABSTRACT

Solar energy, especially through the use of photovoltaic cells, is a promising sustainable energy source for human race. III-V multijunction photovoltaic cells with over 40% confirmed efficiency are among the best candidates for next generation solar cells. However, due to their complex fabrication process, these solar cells are currently too expensive for terrestrial 1 sun use. By using solar concentrators to replace sunlight collection area with cheap materials, total system cost is reduced and cell efficiency is increased. As a result, solar concentrators are viewed as an indispensable part in today's multijunction photovoltaic cell systems.

A novel planar waveguide solar concentrator is proposed in this work. Comparing to conventional solar concentrators, a waveguide is used to output homogenized light onto photovoltaic cells at its end surface. Such a planar structure is potentially easy to fabricate and is possible for novel sun tracking methods. It also benefits in terms of cell connections and heat management.

The basic lens array-waveguide structure with the use of a tapered waveguide as a secondary concentrator shows over 90% efficiency under 800 geometric concentration under ideal cases. Optimizations are applied to the lens array, the couplers, and the secondary concentrator. The optimized structure has <1% geometry loss under 1000 geometric concentration and acceptance angles of 0.5°~0.7° depending on the orientations due to structure asymmetry, which is verified by ZEMAX.

As an integral part, solar tracking methods are reviewed and a two-axis tracking method realized by using a single-axis tracker and lateral translations is studied. Lateral translation is used for adjusting positions for seasonal sun movement. It has two-dimensional x-y tracking instead of horizontal movement x-only. A prototype system of 50 geometric concentration with >75% optical efficiency in simulation and >65% efficiency in experiment is presented as a practical example of the proposed tracking method.

DEDICATION

To my parents

Ziyun Liu and Qiang Liu

To my grandmother

Runfang Song

And to my fiancée

Xiaoyan Li

ACKNOWLEDGEMENTS

I would like to thank my committee chair and my research advisor, Dr. Christi K. Madsen, for her patience, guidance, encouragement, and support throughout my entire graduate study. Her skills and knowledge helped me overcome many difficult situations and finish my dissertation. I would also like to thank other committee members, Dr. Ohannes Eknoyan, Dr. Robert Nevels, and Dr. Alexey Belyanin, for their time and efforts throughout the course of this research.

It has been a great pleasure working with Ran Huang on this project. I am also extremely grateful to my friends in the group, Chen Zhang, Dwayne Macik, Yifeng Zhou, Qi Chen, Xin Wang, and Jae Kim. I want to extend my gratitude to Aggie Fab staff Larry Rehn, Dennie Spears, Robert Atkins, and Jim Gardner for their support and help in the lab.

Finally, special thanks to my family for their unconditional love and support. Thanks to my fiancée. She is the best thing that ever happened to me.

TABLE OF CONTENTS

Page

LIST OF FIGURES

Page

Page

LIST OF TABLES

Page

CHAPTER I

INTRODUCTION

I.1 Solar energy

Electricity is arguably the most convenient and useful type of energy in modern society. It has vast applications ranging from every day use, e.g. light bulbs and home appliance, to novel technologies such as telecommunications and electric cars. The convenience and popularity of electricity also roots in its easy transmission. Electricity is seen as an essential part of civilization and it is indispensable for human race.

However, electricity is a secondary type of energy generated mainly by burning fossil fuel (oil, coal and natural gas). With more people from the so-called developing countries advancing to adopt the high energy consumption life style in today's developed countries, much more energy is required in the future. The reserve of fossil fuel is not unlimited, though. A report from 2008 predicted that oil, coal and gas has approximately 35, 107 and 37 years in reserve, respectively, meaning that coal is available up to 2112, and will be the only type of fossil fuel remaining after 2042 [1]. Furthermore, there exist several environmental issues concerned with fossil fuel combustion. Besides generating air pollutants, e.g. sulfur dioxide and nitrogen oxides, the release of greenhouse gas CO_2 becomes a major problem. Although without conclusive evidence, the climate change including global warming and sea level rise is attributed to the increasing carbon concentration in the atmosphere, to which fossil fuel combustion contributes the most. As a result, alternatives need to be developed soon in place of fossil fuel.

Nuclear energy is viewed as a promising candidate. Nuclear fission plants, generating energy through the transformation of radioactive uranium 235, release no CO_2. It is not considered a clean energy, though, in that the highly radioactive wastes have to be carefully stored for centuries. Another type of nuclear energy, i.e. nuclear fusion, which uses hydrogen isotopes as sources, could be potentially clean and inexhaustible. However, it is still far from any practical application and nuclear energy is inherently dangerous due to its enormous energy intensity.

Solar energy, mainly through photovoltaic (PV) technology, may be the only way out to the stated issues. First of all, energy provided by the Sun arriving on Earth is more than enough. The total solar energy absorbed by Earth ground is approximately $2.7\times10^{24}\,\mathrm{J}$ per year [2]. Using photovoltaics with only 10% conversion efficiency, solar energy can be converted into electricity matching 1000 times the current global consumption [3]. Secondly, photovoltaic industry is clean and safe. The functioning of PVs is free of pollution or waste generation. The manufacture process is also compatible with current semiconductor industries with minor changes. Last but not the least, unlike the unevenly distributed fossil fuels and high-tech nuclear plants, solar energy is accessible to every corner in the world. This is particularly important to those people who are living in under-developed areas without any electricity at all. The construction of a solar farm might be much easier and more practical in these areas, which is a unique property of solar energy. The advantages of photovoltaics are well summarized in [3].

I.2 Principles of photovoltaics

Conceptually, PV cells are a kind of device that converts solar energy into electrical energy. It is usually realized by using semiconductor materials. Semiconductors can absorb light with energy larger than its bandgap E_g and deliver part of the energy to generate electron-hole pairs (carriers). The carefully designed semiconductor device is able to separate the carriers and recombine them through an external circuit, delivering current in a specific direction. An illustration of a simple semiconductor cell is shown in Figure 1. It consists of a pn junction, metallic grids/layers of electrical contacts and an anti-reflection layer.

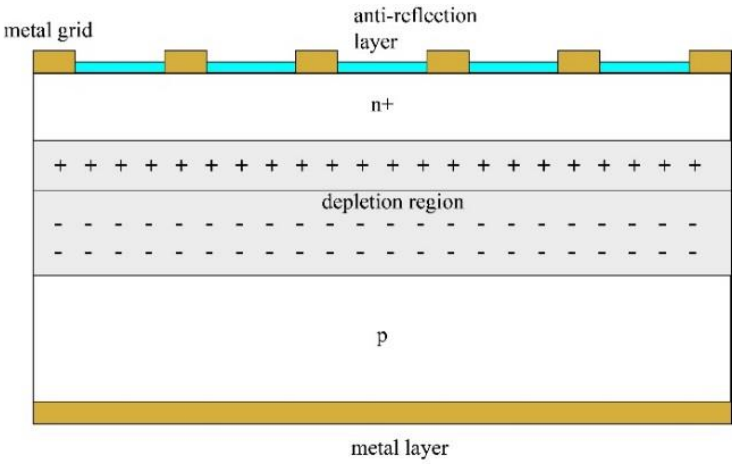

Figure 1. A schematic of a simple semiconductor solar cell made of a pn junction.

Following the physics model built in [4], the I-V characteristic of such a simple cell can be written as

$$I = I_{SC} - I_{o1}\left(e^{qV/kT} - 1\right) - I_{o2}\left(e^{qV/2kT} - 1\right), \tag{I.1}$$

where k is Boltzmann's constant, q is the electric charge of a proton, T is the Kevin temperature, I_{SC} is the light intensity-related short circuit current, I_{o1} and I_{o2} are the dark saturation current due to recombination in the quasi-neutral regions (n^+ and p in Figure 1) and the depletion region, respectively. The macroscopic behavior of a solar cell, therefore, can be modeled using a light controlled current source in parallel with two diodes as shown in Figure 2(a). There are several important parameters when evaluating the performance of a solar cell, namely, short circuit current I_{SC}, open circuit voltage V_{OC}, fill factor FF and conversion efficiency η. These parameters are marked in Figure 2(b). The open circuit voltage is defined as the voltage where there is no current, expressed as

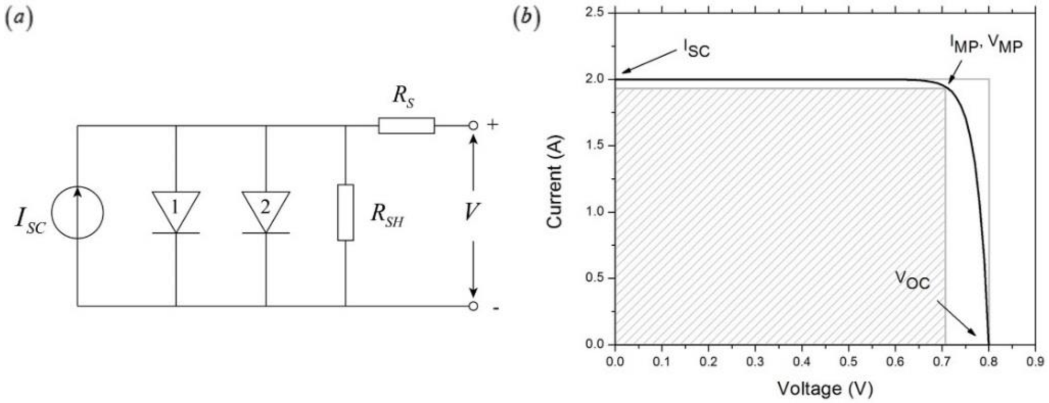

Figure 2. (a) Model of a semiconductor solar cell. The current through diode 1 is $\propto e^{qV/kT}$ and the current through diode 2 is $\propto e^{qV/2kT}$. (b) An I-V curve for an ideal solar cell ($I_{o2} = 0, R_{SH} = \infty$, and $R_S = 0$).

$$V_{OC} \approx \frac{kT}{q} \ln \frac{I_{SC}}{I_{o1}}, \qquad \text{(I.2)}$$

where I_{o2} is omitted and $I_{SC} \gg I_{o1}$. The point where the product of current and voltage, $P = I \times V$, reaches its maximum defines the maximum power point $P_{MP} = I_{MP} \times V_{MP}$. Equivalently, it is the maximum rectangle under the I-V curve, measuring the squareness of the I-V characteristic. Using P_{MP}, the fill factor and the conversion efficiency are defined respectively as,

$$FF = \frac{P_{MP}}{V_{OC} I_{SC}} = \frac{V_{MP} I_{MP}}{V_{OC} I_{SC}}, \tag{I.3}$$

$$\eta = \frac{P_{MP}}{P_{in}} = \frac{FF V_{OC} I_{SC}}{P_{in}}. \tag{I.4}$$

Shunt resistance R_{SH} and series resistance R_S are sometimes included to model the behavior of contacts and parasitic resistance in a real solar cell, as illustrated in Figure 2(a). Eq. (I.1) is therefore modified as

$$I = I_{SC} - I_{o1}\left(e^{q(V+IR_S)/kT} - 1\right) - I_{o2}\left(e^{q(V+IR_S)/2kT} - 1\right) - \frac{V + IR_S}{R_{SH}}. \tag{I.5}$$

The shunt resistance has no effect on short circuit current and conversely the series resistance has no effect on the open circuit voltage. It is worth mentioning that when the current is large, power dissipated on the series resistance $P = I^2 R_S$ can be a major loss source.

Temperature plays another important role as the dark saturation current $I_{o1} \propto n_i^2$ and $I_{o2} \propto n_i$, where n_i is the intrinsic carrier concentration. n_i itself is also a function of temperature T

$$n_i \approx \frac{2\left(2\pi kT\right)^{3/2}}{h^3}\left(m_n^* m_p^*\right)^{3/4} T^{3/2} e^{\left(\frac{\alpha T^2}{T+\beta} - E_g(0)\right)/2kT}, \qquad \text{(I.6)}$$

where h is Plank's constant, m^*s are effective mass of electrons and holes, α and β are constants. As temperature increases, the intrinsic carrier concentration increases and so does the dark saturation current. It is therefore desired to keep the cell temperature as cool as possible, which is a crucial factor in the design of concentrator cells.

I.2.1 Crystalline silicon solar cells

Crystalline silicon cells are the dominating type of solar cell in today's market, benefiting from the maturity of the silicon based microelectronic manufacture industry. The manufacturing process of silicon cells can use these techniques with only minor modifications, leading to lower initial cost. Silicon is abundant, stable, clean, and more importantly, the bandgap of 1.1eV matches well with the optimal point on the solar spectrum. The matching bandgap with solar spectrum is crucial for solar cells, whether single junction or not, since semiconductor materials are transparent to photons with energy less than the bandgap and excess energy above the bandgap is lost in the form of heat. In 1960, W. Shockley and H. Queisser pointed out the theoretical efficiency upper limit (SQ efficiency limit) for a pn junction solar cell, using detailed balancing theory, to be ~30% for 1.1V bandgap when the Sun is assumed to be an ideal blackbody at 6000K and the cell at 300K [5]. Silicon is an optimal selection for single junction cells.

Despite the theoretical efficiency for silicon cells, the practical efficiency falls from 13% to 17% for cells fabricated by the Czochralski technique [3]. Moreover, due to the indirect bandgap in silicon, it absorbs sunlight weakly and thick cells are required as a result, setting a high standard for impurity and perfection levels. Consequently, increasing efficiency and reducing manufacture cost are the main drivers in silicon solar cell industry now, which is not easy to realize. III-V multijunction solar cells, with much larger efficiency upper limit, are promising for next generation photovoltaics.

I.2.2 High efficiency III-V multijunction solar cells

The design of multijunction solar cells is rather straightforward. Instead of using only one material, multiple layers of materials with different bandgaps (E_{g1}, E_{g2}, …, E_{gn}) are stacked together, each absorbing a particular range of the solar spectrum. The top material is always with the largest bandgap, which absorbs photons with energy from E_{g1} to ∞; while the second layer absorbs photons with energy from E_{g2} to E_{g1}; after all the layers, only photons with energy smaller than E_{gn} are not absorbed. If there is an infinite number of layers ($n \to \infty$), the theoretical efficiency would be as high as 86.8%, reaching the ideal converter efficiency limit between 6000K and 300K [6]. However, most of the practical structures have only two or three layers, because fabrication issues such as lattice matching and different heat expansion coefficients become significant when more layers come into play. Fortunately, the efficiency boost by adding layers is the most from one to two layers, changing from ~37% to 50% [7].

III-V materials are among the best candidates for multijunction cells. Their easily tunable bandgaps, good lattice matching, relatively easy fabrication, and straightforward doping process make them promising for next generation solar cells. Currently confirmed multijunction solar cell efficiency lies around 44% [8] using either 3-junction cell architectures GaInP/GaAs/GaInAs (inverted metamorphic, Sharp [9]) and

GaInP/GaAs/GaInNAsSb (dilute nitride, Solar Junction [10, 11]) to replace the Ge bottom cell to better match the generated current, or 4-junction cell architectures GaInP/GaAs/GaInAsP/GaInAs (wafer bonding, Fraunhofer ISE & Soitec [12]) and GaInP/GaAs/GaInAs/GaInAs (inverted metamorphic, NREL [13]). The spectral response is approximately from 350nm to 1350nm for 3-J cells and from 350nm to 1750nm for 4-J cells. Under concentration, the high efficiency 44% can be maintained from 400X to 600X in [9], 43.5% from 400X up to 925X in [10], 44.7% at 297X in [12], and 43.8% at 327X in [13], where X represents irradiance level at X suns describing the optical concentration factor C_{opt} and one sun (1X) is defined as $1000W/m^2$, AM1.5D, ASTM G173-03. A summary of these cell performances is shown in Table 1.

Table 1. A summary of the cell performances.

References	**[9]**	**[11]**	**[12]**	**[13]**
Highest Efficiency	400X-600X, 44%	400X-600X, 43.5%	297X, 44.7%	327X, 43.8%
Highest Concentration	1000X, >42%	925X, 43.5%	962X, 42.6%	869X, 42.9%

Unfortunately, due to the much more complex design and fabrication process, although they prove successful in space applications, III-V multijunction cells are currently too expensive for terrestrial one sun uses. This leads to the development of concentrator photovoltaics. By incorporating with solar concentrators, the projected cost can be reduced, which makes III-V multijunction solar cells very attractive for future terrestrial applications.

I.3 Solar concentrators

I.3.1 Why solar concentrators

One single important driver for the development of solar concentrators, as stated before, is to reduce the cost of expensive solar cells. In a solar concentrator system, the sunlight collection area is replaced by the concentrator material, which is always a lot cheaper than solar cells. As a result, with the same cell surface area, more sunlight is collected and thus the cost is reduced. A simple model is built to illustrate the cost reduction [14]

$$Cost\left(\$/kWh\right) = \frac{C.C.\left(\$/m^2\right) + \dfrac{Cell}{\mathrm{X}}\left(\$/m^2\right)}{E_{in}\left(kWh/m^2\cdot year\right)\cdot \eta_{sys}} \times ADR \tag{I.7}$$

where $C.C.$ is the cost of concentrator, $Cell$ is the cost of the solar cell, E_{in} is the energy collected per m^2 in a year, η_{sys} is the total system efficiency (conversion from solar energy to electrical energy) and ADR is the annual discount rate. It is evident that a successful concentrating system should be cheap for construction, of high concentration, and yet offers high efficiency.

Besides the reduced cost, the operation of solar cells under concentrated sunlight with X times illumination leads to an increase in efficiency, approximately given by

$$I_{SC}^{X} = \mathrm{X} I_{sc}^{1}, \tag{I.8}$$

$$V_{OC}^{\mathrm{X}} = V_{oc}^{1} + \frac{kT}{q}\ln \mathrm{X}, \text{ and} \tag{I.9}$$

$$\eta = \frac{FF^{\mathrm{X}} V_{OC}^{\mathrm{X}} I_{SC}^{1}}{P_{in}} = \eta^{1}\left(\frac{FF^{\mathrm{X}}}{FF^{1}}\right)\left(1 + \frac{\dfrac{kT}{q}\ln \mathrm{X}}{V_{OC}^{1}}\right). \tag{I.10}$$

Although Eqs. (I.8)~(I.10) use the simplest model based on a single-junction solar cell, more complex models including series resistance and temperature dependence suggest similar trends [15]. The efficiency goes up only to a point where cooling becomes an issue, FF begins to drop and the large current brings huge loss on series resistance. Referring to Table 1, the highest efficiencies are all within 300X-600X and the cell designs aim to maintain high efficiency up to 1000X, mainly from an economic point of view. The desired concentration range in this work is 500~1000.

I.3.2 Figures of merit

Concentration is the most important characteristic for a concentrator system. While optical concentration C_{opt} defined above describes the irradiance level, geometric concentration C_{geo} is a more straightforward design parameter that specifies the surface area ratio between input and output apertures of a solar concentrator system. Optical concentration can then be readily derived from the product of C_{geo}, the optical efficiency η, and the available local direct sunlight irradiance E,

$$C_{opt} = C_{geo} \times \eta \times \left[E / 1000\left(W / m^2\right) \right]. \tag{I.11}$$

The higher the efficiency is, the closer the optical concentration is to the geometric concentration under standard test conditions.

Except for concentration and efficiency, angular acceptance (or acceptance angle) is another crucial factor in the design of concentrators and it is closely related to the maximum possible achievable concentration. Angular acceptance is defined as the field of view seen by the input aperture (Figure 3). The theory of etendue [16], proved by thermodynamics theory, states that the product of the area (physical space) and the input/output angle (angular space) of an optical system is an invariant in an ideal system. As a result, any concentration is achieved at the expense of increased output angle. When the output angle reaches $\pm 90°$, geometric concentration arrives at its maximum, given by

$$C_{2D\max} = \frac{n}{\sin\theta} \text{ (for 2D optics), and} \tag{I.12}$$

$$C_{3D\max} = \frac{n^2}{\sin^2\theta} \text{ (for 3D optics),} \tag{I.13}$$

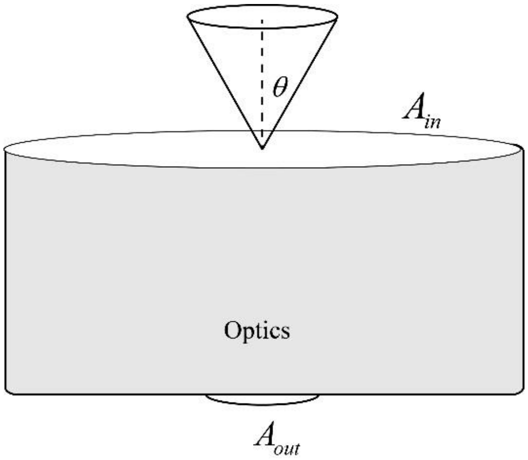

Figure 3. Illustration of etendue.

where n is the refractive index of the output space, assuming the input is air. Hence the larger the angular acceptance θ is, the smaller the achievable concentration $C_{\max}$. The theoretical smallest angular acceptance for a solar concentrator system is the sunlight incident angle onto Earth, i.e. $\pm 0.266°$. The maximum concentration one can have is then 212X for 2D and 45032X for 3D, respectively. In practical applications, the ±0.266° can never be exactly met and a certain margin is always taken into consideration in the design of concentrators. This angular acceptance is a unique property of a concentrating system in comparison to a conventional silicon based system. It requires the system normal pointing at the direct sunlight all the time (through the use of a solar tracker) to make sure such tracking error is within the angular acceptance.

Uniformity, i.e. the distribution of the light intensity onto solar cells, is also important for concentrator photovoltaics. By introducing optical elements into the solar system, the distribution of sunlight intensity is modified and non-uniform illumination on photovoltaic cells is generated. The presence of non-uniform illumination can have two main effects [17]. Electrically, there is excessive illumination on a portion of the solar cell surface, resulting in an internal current flowing even in open-circuit conditions. It leads to wasted energy in the form of heat. Thermally the generated heat causes hot spots in the solar cell, increasing local temperature. The temperature increase negatively impact the cell efficiency as described in Eq. I.6. These two combined effects lower the total cell efficiency. Several groups studied the effect of non-uniform illumination on concentrating photovoltaic cells both theoretically and experimentally. For example, Araki and Yamaguchi studied a distributed circuit model and calculated the efficiency drop for a triple junction cell using a Gaussian intensity profile with included chromatic aberration [18]. An obvious reduction on I_{sc} and FF can be observed. Similarly, Herrero et al. [19] and Victoria et al. [20] experimentally investigated the influence of non-uniformity on the FF of III-V solar cells. A relative FF decrease of 0.16 is measured for a Fresnel/Cell structure with intensity Peak-Average-Ratio (PAR) of 10 [19] and such drop is expected to increase as the concentration increases.

Finally, it is desired the optics before the solar cell does not change the solar spectrum and brings no chromatic aberration. The bandgaps in multijunction cells are always tuned in accordance to the incoming spectrum to maximize the conversion efficiency. Hence any deviation from the designed spectrum impairs the cell efficiency.

I.3.3 Typical concentrator designs

I.3.3.1 Compound parabolic concentrators

Using edge-ray principle, R. Winston for the first time developed an ideal 2D concentrator [21], called a compound parabolic concentrator (CPC), reaching the theoretical upper limit of etendue. The output ray angles, as expected, covers the full range of $\pm 90^\circ$. This type of concentrators, although remarkable in the designs, have limited practical applications considering the materials used in construction from an economic point of view. The aspect ratio (height over collection aperture) is also too large, which sets high standard for the supporting structures due to the enormous wind load. Hence a truncated version of CPC is always used in trade of lower efficiency [22].

I.3.3.2 The Fresnel lens

Fresnel lenses are the most popular concentrator type in today’s concentrator market. It is compact, cheap, easy to design, and yet offers acceptable concentration and efficiency. The concept of Fresnel lenses is straightforward. The phase change in a conventional lens is approximated by the prisms in the Fresnel lens and thus offers similar performance (Figure 4). Comparing to conventional lenses, the Fresnel lens is thin and cheap (usually made of plastic materials), which is a big advantage for small f-numbers ($f/\#$, defined as the ratio of focal length f over the lens diameter D). When the image quality is not critical, Fresnel lenses might be better a choice.

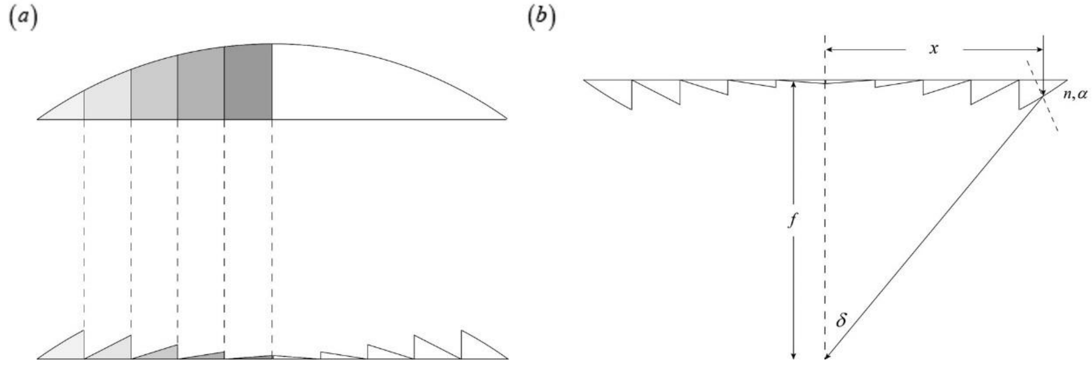

Figure 4. (a) A Fresnel lens approximates the phase change of a conventional lens. It offers a compact design in trade of image quality. (b) The construction of a simple Fresnel lens.

Figure 4(b) shows the construction of a simple Fresnel lens. The grooves are usually placed inward towards the receiver so that the features can be better protected from environmental factors for the purpose of maintenance. Assuming normal incidence, light will only be refracted once. Using Snell's law and basic geometry, the prism angle can be calculated as

$$\alpha = \arctan \frac{x/f}{n\sqrt{(x/f)^2+1}-1}, \tag{I.14}$$

where x is the center position of each prism, f is the focal length, and n is the refractive index of the lens material. Eq. (I.14) also assumes the height and width of each prism (pitch) is much smaller than the whole lens structure. The smaller the pitch is, the better the image quality. Considering the incoming light has $\theta_s = \pm 0.27°$ divergence angle, the spot size diameter at the focal point is approximately given by

$$\Delta = 2\theta_s f \left(1 + \frac{D^2}{4f^2}\right). \tag{I.15}$$

When $f/\# = 0.5$, the ratio between the spot size Δ and diameter D is minimized; therefore small f-number is desired. However, small f-number always leads to larger convergence angle, where Fresnel reflection at the prism/air surface might be a problem; it is therefore not possible to make Fresnel lenses with $f/\# < 0.9$ [23], setting an upper limit for the concentration ability given the lens diameter. Another issue related to refracting optics is the dispersion of the lens material, chromatic aberration presents at the focal point. To solve these problems, secondary concentrators are often incorporated together with concentrating systems using lens as the primary concentrator.

I.3.3.3 Secondary concentrators

A secondary concentrator is used in subsequence with the primary concentrator to further increase concentration, as long as the primary concentrator is not ideal. Different designs are proposed for secondary concentrators, e.g. reflective cones, CPCs, reflective pyramids and waveguides. Most of the secondary concentrators are non-imaging devices and are desired to homogenize the output light. Waveguides, which use total internal reflections (TIRs) to guide light, is an attractive concentrator, because it is a planar device that can be fabricated using cheap techniques. Moreover, waveguides are inherent homogenizers, offering output light with great uniformity.

I.3.4 The ultimate goal of solar concentrators

The ultimate goal of solar concentrators for the use of III-V multijunction solar cells is to efficiently generating concentrated sunlight that is required by the effectiveness of the solar cells, with little spectrum interference, using cheap materials and fabrication techniques. Such a solar system is able to function effectively, economically and sustainably. The properties of a good concentrating photovoltaic (CPV) system are summarized below:

- Achieve >500X concentration with high efficiency
- Optical transparent in the working wavelength range (from ~350nm to ~1.75μm)
- Uniform output
- Large angular acceptance (important for tracking design)
- Cheap for fabrication
- Easy for maintenance

I.4 The scope of this work

A typical CPV system consists of concentrating optics, concentrating photovoltaic cells, thermal management system, supporting structures, and tracking mechanisms. While the construction of an entire system requires interdisciplinary knowledge, including optical, electrical, and mechanical engineering, the work presented in this dissertation mainly focuses on the optical designs of a planar waveguide solar concentrator. Design and simulation works are discussed in great details, while preliminary fabrication and measurements are also briefly introduced. Compatible tracking methods are included as an essential element in the design. However, the detailed modelling of the concentrating photovoltaic cells, the cooling system, the connections between the building blocks, and the design of supporting structures are beyond the scope of this work and will be in the future plans of this project.

CHAPTER II

PLANAR WAVEGUIDE SOLAR CONCENTRATORS

II.1 Introduction

In 2010, a new approach of CPV systems was proposed by Karp et al. for a planar concentrating structure [24], where a single slab waveguide is used as a homogenizer incorporated with a lens array as the primary concentrator. Solar cells are all placed at the output ends of the waveguides, and therefore alleviates connection and cooling issues usually associated with concentrator designs. Sunlight is first collected by a lens array and then coupled into the waveguide by a series of microstructure at each focal point of the lenses. Then the coupled light travels inside the slab waveguide by total internal reflections (TIRs) and finally exits from both edges directly onto PV cells. Recently, several other designs use similar ideas, too. These planar waveguide concentrator designs are cheap to fabricate, output uniform light and are relatively efficient at high concentration. In this chapter, Karp's design will first be carefully reviewed; then other proposed configurations are briefly discussed. By summarizing the advantages and disadvantages of these designs, the motivation of developing a new planar waveguide concentrator is made clear.

II.2 Karp's first design

Figure 5 shows the biggest difference between the waveguide concentrator design and a traditional concentrator system. In a traditional concentrator system, whether using secondary optics or not, hundreds of solar cells are individually placed in accordance with their own optical components; in contrast, light collected by the lens array propagates inside a waveguide and solar cells are placed at the end of the waveguide only in a planar waveguide concentrator. It is therefore much easier to design associated cooling and interconnecting structures. Moreover, waveguides are inherent homogenizers and TIRs are not wavelength sensitive. Uniform output with no chromatic aberrations can be expected.

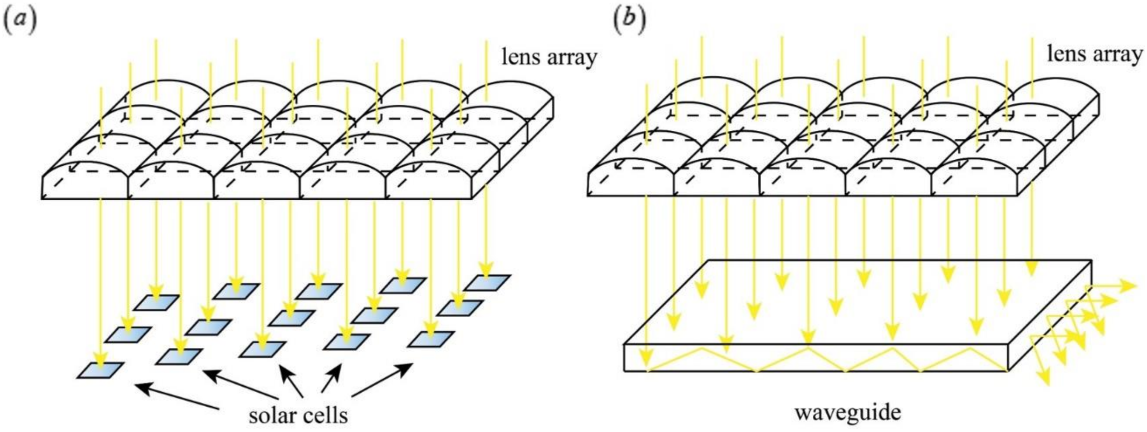

Figure 5. A basic structure of (a) a traditional concentrator system; (b) a slab waveguide concentrator.

Karp's design consists of three main parts: a lens array, couplers and a slab waveguide (Figure 6). The geometric concentration of the system is

$$C = \frac{W \times L}{H \times W} = \frac{L}{H}, \tag{II.1}$$

where W is the width of the system and it does not play any role in this configuration. As the length L increases or the waveguide thickness H decreases, the concentration would increase. However, as would be stated later, the increase of concentration is in trade of lower efficiency. At some point, the efficiency is so low that the whole structure becomes meaningless.

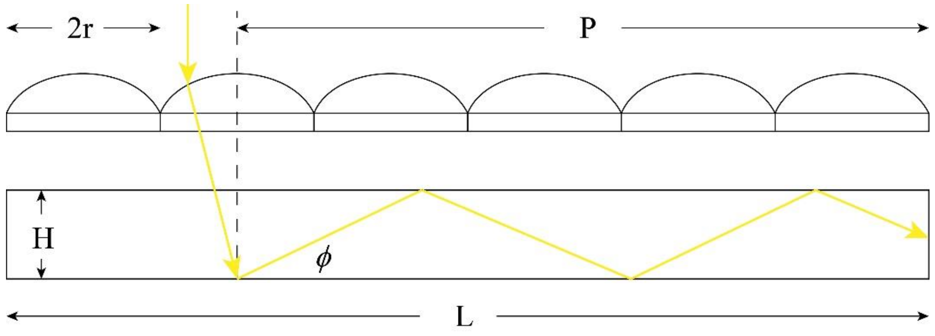

Figure 6. The geometry associated with Karp's planar waveguide concentrator.

Light traveling in the waveguide may be decoupled as it hits subsequent coupling features, leading to the main loss mechanism in this design. Consider a 2D math model. A beam of light is collected at P and reflected into the waveguide with angle ϕ by the couplers. The light would encounter $\frac{P\tan\phi}{2H}$ times of reflection at the bottom of the waveguide. Therefore the chance that such a light beam should not be decoupled is

$$\eta_{decouple}\left(P,\phi\right)=\left(1-\frac{1}{C_{lens}}\right)^{\frac{P\tan\phi}{2H}}, \tag{II.2}$$

where C_{lens} is the concentration ratio by the lens array and thus $1/C_{lens}$ represents the fraction of decoupling area inside the waveguide. . Considering the decoupling loss, the reflecting loss at interfaces R (including Fresnel reflections and coupler reflectance), the propagation loss $e^{-\alpha P/\cos\phi}$, the optical efficiency for a specific P and ϕ can be expressed as

$$\eta(P,\phi)=(1-R)\times\eta_{decouple}(P,\phi)\times e^{-\frac{\alpha P}{\cos\phi}}=(1-R)\times\left(1-\frac{1}{C_{lens}}\right)^{\frac{P\tan\phi}{2H}}\times e^{-\frac{\alpha P}{\cos\phi}}. \quad \text{(II.3)}$$

Summing up all the lenses and angles, the mean optical efficiency of the whole system would be given by

$$\begin{aligned}\bar{\eta}&=\frac{\sum_{P}\frac{\int_{\phi_i}^{\phi_f}\eta(P,\phi)d\phi}{\phi_f-\phi_i}}{L/2r}\\&=\frac{(1-R)}{L/2r}\times\sum_{P}\frac{\int_{\phi_i}^{\phi_f}\left(1-\frac{1}{C_{lens}}\right)^{\frac{P\tan\phi}{2h}}\times e^{-\frac{\alpha P}{\cos\phi}}d\phi}{\phi_f-\phi_i},P=r,3r,5r,...L-r.\end{aligned} \quad \text{(II.4)}$$

C_{lens}, ϕ_i and ϕ_f are determined by the angular acceptance δ, the lens f-number and the coupler angle. The detailed modeling of a lens array can be found in Chapter III. Meanwhile in [24], Karp chooses $\beta=30°$ to be the coupler angle mainly from fabrication considerations. As their coupler is composed of a series of microstructures at each focal point, instead of only one reflecting surface, the coupler angle has to be small enough ($\beta\leq 30°$) so that reflecting light do not hit the neighbor coupler and be decoupled immediately (Figure 7).

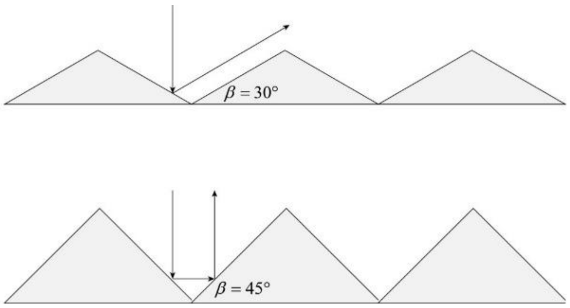

Figure 7. The coupler angle has to be small in order to avoid immediate decoupling from the neighbor coupler.

Figure 8 illustrates the optical dependence on several parameters as indicated in Eq. (II.4). An $f/3$ lens array with $\delta = 0.27°$ incident angle and coupler $\beta = 30°$ is assumed in Figure 8(a). It is evident that the optical efficiency drops dramatically when the thickness H is reduced. It indicates that the decoupling loss is the most important issue associated with this design, leading to lower efficiency when the concentration is high. Meanwhile, the angular acceptance is also limited in that it also has an effect on the coupler size and hence influences the decoupling loss. In these plots, all reflections are assumed ideal. The aluminum reflective microstructures, in reality, have reflectance below 90%. Therefore the practical performance falls even below the simulation numbers. Although 81.9% efficiency at $C_{geo} = 300$ and 44.8% efficiency at $C_{geo} = 37.5$ concentration are simulated, only 32.4% efficiency is measured in the fabricated 37.5X prototype.

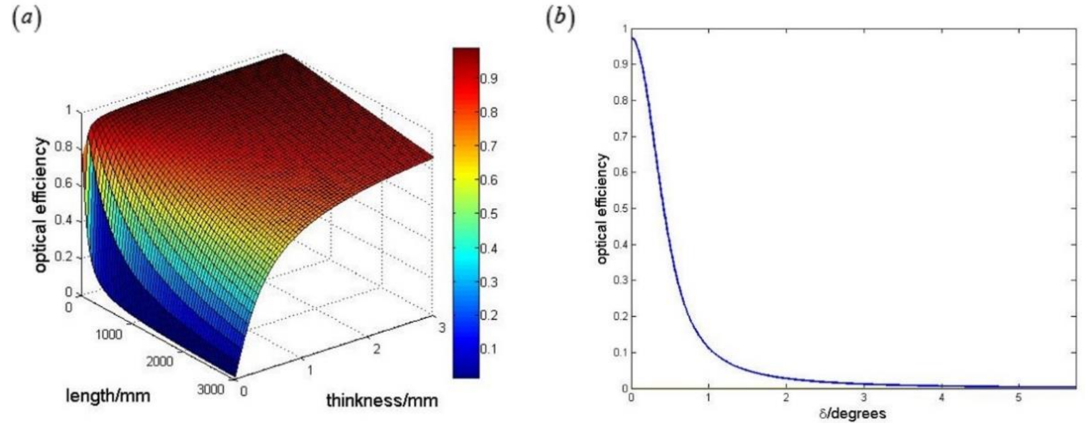

Figure 8. Optical efficiency as a function of (a) waveguide length and thickness; and (b) target tolerance angle.

Karp published his subsequent study using orthogonal waveguides and secondary optics design to further boost the performance of the proposed structure [25]. The measured efficiency is significantly smaller than the expected ideal values due to the complicated configurations. The decoupling loss mechanism is inherent and better designs are needed.

II.3 Other designs

W. Shieh and G. Su proposed an almost exactly the same structure in 2011 [26], except for the microstructure couplers are replaced by the idea of $25°$ mirror prisms. They also very briefly discussed issues concerned oblique incident angles up to $10°$. This structure has no advantage over Karp's design. The waveguide is still lossy and no device is fabricated because the prism structure is hard to realize.

S. Bouchard and S. Thibault published their work based on line-focus primary concentrators [27], namely replacing the lens array with cylindrical lens arrays, mainly for tracking purposes. The also use unsymmetrical coupler designs to better couple light with different angles into the waveguide. Again, the inherent lossy waveguide remains the same with Karp’s design. As a result, although their proposed structure is within the <10X range, only 78% efficiency can be achieved.

S. Chu et al. use a saw tooth shape waveguide to alleviate the decoupling problem [28, 29]. The main difference is the shape of their couplers. Their design consists of an injection element and a bypass element. Light is coupled into the waveguide by the injection part; and whenever light already in the waveguide hits the bypass element, it gains a small angle rather than directly decoupled out in Karp’s configuration. However, such a coupler design leads to wider waveguides and thus decreases concentration. No practical device measurement results are reported as the whole design is complex and the coupler shape might be an issue in real fabrications.

An inspiring idea was proposed by I. Fujieda et al. using branched planar waveguides [30, 31]. Light is still coupled into waveguides by couplers but TIR instead of metallic reflector is used. Also, they completely eliminate the decoupling loss inside the waveguide by using a “stem + branch” structure. A tapered stem acts as the main light guiding path while light is collected through branched collectors. Double TIR coupling features orthogonal to each other are used, namely one directs light from lens to waveguide, and the other changes the propagation direction of light. The loss mechanism is mostly from Fresnel reflections, in contrast of decoupling losses associated with previous design, which is the biggest the advantage of this setup. However, the number of unit structure is limited because the angle of propagation light would increase as traveling inside a tapered waveguide. Furthermore, the double reflection surfaces is too complex to be accurately modeled; and the unit sample fabricated does not show good match with the predicted efficiency due to fabrication difficulties.

D. Moore et al. and Selimoglu et al. studied the behavior of a promising stepped waveguide structure [32-34]. In this design, the couplers are laterally/vertically displaced in order to avoid decoupling. The output light can be further concentrated using secondary optics. This structure eliminates any possible decoupling loss in the waveguide and high efficiency can be expected at high concentration. General discussion are presented in the references. However, due to the lack of detailed math models, they fail to point out several important parameter tradeoffs in this design, which are crucial in terms of the waveguide performance. Moreover, the proposed secondary optics incorporated with the waveguide are hard to realize and thus no device level fabrication result has yet published.

II.4 Motivations of developing a novel planar waveguide solar concentrator

A thorough study of a novel planar waveguide solar concentrator is presented in this work, following the discussions in [32-34]. The aim is to design a solar concentrator structure that provides >500 concentration, high efficiency, uniform output and little spectrum distortion. The proposed structure is easy to fabricate with cheap materials and compatible with III-V multijunction solar cells. In Chapter III, the basic system is introduced, a detailed math model is built and parameter tradeoffs are carefully examined. In Chapter IV, several optimizations are applied and discussed. Chapter V briefly introduces some preliminary experimental results, including fabrication process and measurement setups. As an integrated part of a solar concentrating system, the Sun movement, conventional solar trackers, and novel solar tracking methods that are specifically designed for planar concentrators are presented in Chapter VI. Summary and future works are included in Chapter VII.

CHAPTER III

DESIGN OF A PLANAR WAVEGUIDE SOLAR CONCENTRATOR*

III.1 System overview

The proposed structure is composed of mainly a lens array and waveguides. Figure 9 illustrates an overview of the lens-to-channel waveguide system. It consists of an $M \times N$ square lens array and corresponding channel waveguides. The end of each waveguide is angled, which acts as a coupler at the focal point of each lens, redirecting light into the waveguide. The lens axes M-N are tiled at an angle Θ with respect to X-Z plane. As a result, the channel waveguides are closely packed and no gap exists between any of the waveguides. Theoretically the sidewalls between neighbor waveguides are transparent; light will mix and all channel waveguides become one single structure. In this setup, light already in waveguides has no chance of hitting subsequent couplers before it couples directly to PV cells.

---

* Part of this chapter is reprinted with permission from "Design of a lens-to-channel waveguide system as a solar concentrator structure," Y. Liu, R. Huang, and C. K. Madsen, *Optics Express*, vol. 22, pp. A198-A204, 2014, copyright 2014 by OSA.

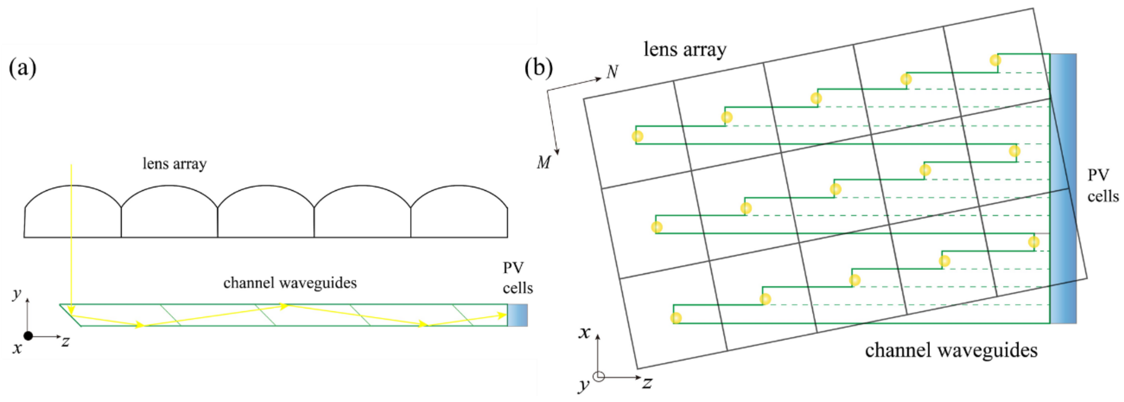

Figure 9. The proposed structure (a) side view; and (b) top view.

Figure 10 is a detailed view of the lens array and the waveguides. Each lens is a $D \times D$ square. When light goes through the lens, it is focused at the focal plane of the lens with a spot diameter d. In order to contain all light, the minimum waveguide width W is $W_{\min} = d$. Therefore the output area is expressed as

$$A_r = M \times N \times W \times t \xrightarrow{\min} M \times N \times d \times t, \tag{III.1}$$

where t is waveguide thickness. The geometric concentration ratio C_1 is

$$C_1 = \frac{M \times N \times D^2}{A_r} = \frac{D^2}{W \times t} \xrightarrow{\max} \frac{D^2}{d \times t}. \tag{III.2}$$

It is interesting to note that the concentration ratio totally depends on the properties of individual lenses and waveguides, i.e. D, W (or d), and t. Hence the lens-to-channel waveguide structure can be viewed as a replica of individual lens-waveguide pairs.

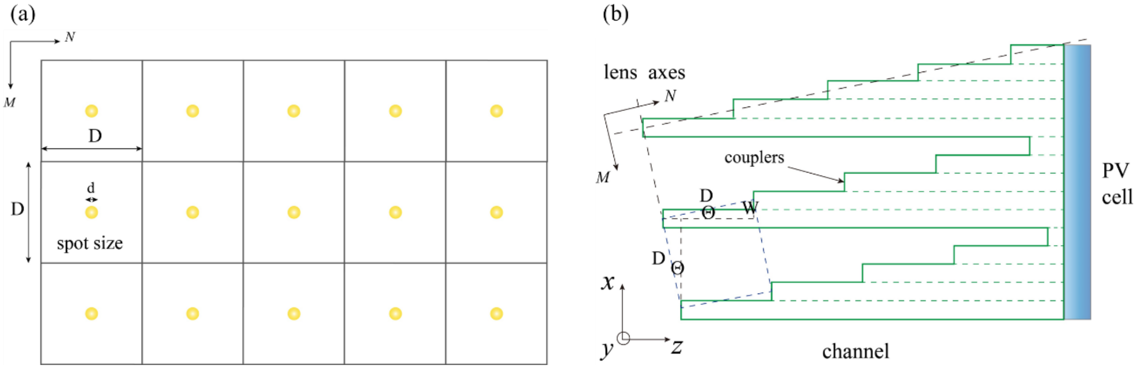

Figure 10. A detailed view of (a) the lens array; and (b) the channel waveguides.

While M can be any arbitrary values, N is limited by the ratio of lens size and waveguide width (and thus by the ratio of lens concentration D/d), as Figure 10(b) suggests,

$$N = \frac{D}{W} \times \cos\Theta = \cot\Theta, \text{ or} \tag{III.3}$$

$$N = \sqrt{\frac{D^2}{W^2} - 1}, \tag{III.4}$$

where the lens tilting angle

$$\Theta = \arcsin\frac{W}{D}. \tag{III.5}$$

Again, these parameters are also determined by individual lens and waveguide properties. In summary, as long as D, W (or d), and t are known, the whole structure can be constructed as the following steps:

- Determine the number of lenses in a row N according to Eq. (III.4);
- Determine the tilting angle Θ according to Eq. (III.5);

- Select any M according to the desired output area calculated by Eq. (III.1);
- Aim the center of one lens to the center of its corresponding channel waveguide; the whole structure would be automatically aligned.

It is worth mentioning that W is always set as close to the minimum value $W_{\min} = d$ as possible and that makes N an integer at the same time. The maximum concentration is achieved in this way.

III.2 Optical designs

In order to examine the relations between the lens diameter D, the spot size d, and the waveguide thickness t as well as to estimate optical efficiency, each component, i.e. the lens array, the couplers, and the waveguides, is separately modeled.

III.2.1 The lens array

Only first order properties of a lens are used in the calculations in that higher order aberrations do not play an important role in determining the spot size or angular distribution in a single lens system for small incident fields, unless under extreme conditions (e.g. lens with $f/0.5$). Although the concept of f-number is usually associated with only a circular aperture with diameter D, it is extended here for rectangular lenses as the ratio between its focal length f and its side length D. Assuming the lens D is thin, a simple meridional plane ray tracing is shown in Figure 11. When the incoming field has a maximum half angle δ_M, it is focused onto the imaging plane, leaving a spot size of

$$d = 2f \tan \delta_M . \qquad \text{(III.6)}$$

In this sense, the concentration from the lens is

$$C_{lens} = \frac{D^2}{\pi d^2/4} = \frac{D^2}{\pi f^2 \tan^2 \delta_M} = \frac{1}{\pi \left(f/\# \right)^2 \tan^2 \delta_M}. \tag{III.7}$$

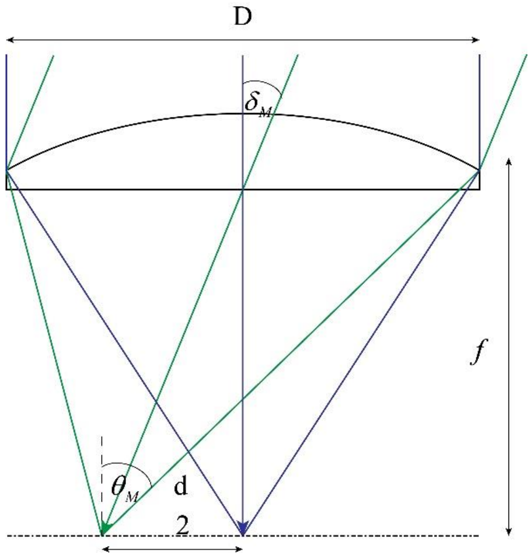

Figure 11. Light is focused onto the imaging plane.

It is evident, as a result, a small f-number is desired for the lens array. However, as mentioned in I.3.3.2, lenses with f-numbers smaller than 0.9 is impossible to achieve and aberrations become a major problem that Eqs. (III.6) and (III.7) do not hold any more. Comparing to the 3D etendue limit given by Eq. (I.13), a simple square lens is approximately $\frac{1}{\pi \left(f/\# \right)^2}$ times the power of an ideal concentrator, where a small incident angle is assumed ($\delta_M \sim \sin \delta_M \sim \tan \delta_M$).

Except for the spot size, the angular distribution after the lens is another important parameter. Define the edge ray in this lens system θ_M as the ray with maximum angle with respect to lens optical axis as shown in Figure 11, which is expressed as

$$\theta_M = \arctan\left(\tan\delta_M + \frac{D}{2f}\right) = \arctan\left(\tan\delta_M + \frac{1}{2f/\#}\right). \qquad \text{(III.8)}$$

Clearly, f-number is the dominating factor in this equation when δ_M is small. When f-number decreases, the edge ray angle θ_M increases, as expected from conservation of etendue.

Although sunlight uniformly illuminates the whole lens aperture, there exists a hot center at the focal plane (Figure 12).

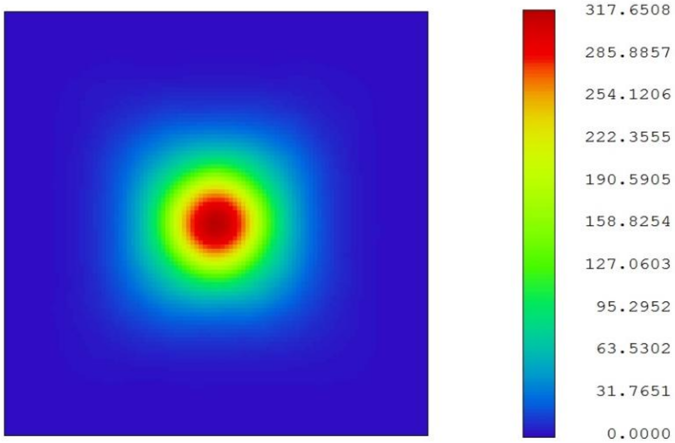

Figure 12. A typical irradiance distribution at the lens focal plane.

III.2.2 Couplers

Couplers are used for redirecting light after the lens array into guided modes of channel waveguides. The end of the waveguide is angled so that light is reflected when hitting this surface. Consider a beam of light after the lens array. The light is expressed using its angles in a spherical coordinate system (θ,φ), where $-\theta_M \le \theta \le \theta_M$ and $0 \le \varphi < 2\pi$. It will be first refracted at the air ($n=1$) /cladding (n_c)/waveguide (n_w) interface before hitting the coupler. According to Snell's law, $\sin\theta = n_w \sin\gamma$. Using angle definitions in Figure 13, incident light (θ,Ω) onto the coupler surface is expressed as

$$\vec{k_i} = (\sin\gamma\cos\Omega, \cos\gamma, \sin\gamma\sin\Omega), \tag{III.9}$$

where the sign of $\vec{k_i}$ is omitted (light is in fact reversed in Eq. (III.9) according to the angle definitions in Figure 13). Meanwhile, the coupler normal is

$$\vec{n} = (0, \cos\beta, \sin\beta), \tag{III.10}$$

where β is the coupler angle with respect to the z axis.

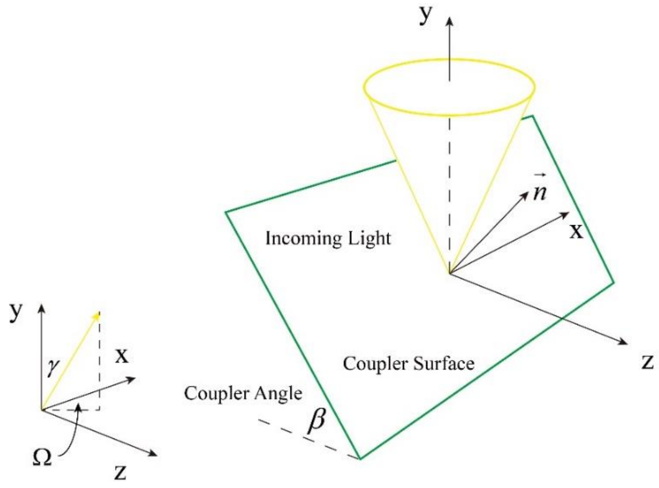

Figure 13. Definitions of angles at the coupler surface.

Combining Eqs. (III.9) and (III.10), the incident angle is calculated as

$$\phi_i = \arccos\left(\overrightarrow{k_i} \cdot \vec{n}\right) = \arccos\left(\cos\beta\cos\gamma + \sin\beta\sin\gamma\sin\Omega\right). \qquad \text{(III.11)}$$

If the coupler surface is not coated by metallic materials, TIR condition has to be fulfilled by Eq. (III.11), i.e.

$$\phi_i \geq \phi_{c-cp} = \arcsin\frac{1}{n_w}. \qquad \text{(III.12)}$$

Light violating Eq. (III.12) is lost in these scenarios, leading to reduced efficiency. Similarly through some vector manipulations, the reflected light into waveguide $\overrightarrow{k_r} = \left(k_{rx0}, k_{ry0}, k_{rz0}\right)$ is expressed as

$$\overrightarrow{k_r} = \left(\sin\gamma\cos\Omega, \cos\chi\sqrt{1-\sin^2\gamma\cos^2\Omega}, \sin\chi\sqrt{1-\sin^2\gamma\cos^2\Omega}\right), \qquad \text{(III.13)}$$

where $\chi = 2\beta - \arctan\left(\tan\gamma\sin\Omega\right)$. Again, TIR conditions for x axis (sidewalls) and y axis (cladding and substrate) are, respectively

$$\text{x axis: } \arccos k_{rx0} \geq \phi_{c-sw} = \arcsin\frac{1}{n_w}, \tag{III.14}$$

$$\text{y axis: } \arccos k_{ry0} \geq \phi_{c-s/c} = \arcsin\frac{\max\left(n_s, n_c\right)}{n_w}. \tag{III.15}$$

$\max\left(n_s, n_c\right)$ in Eq. (III.15) represents the larger refractive index between n_s and n_c, namely the limiting factor for y axis TIRs. Light should also be able to reach the receiver (n_r) from the output end of the waveguide,

$$\text{z axis: } \arccos k_{rz0} < \phi_{c-r} = \arcsin\frac{n_r}{n_w}. \tag{III.16}$$

An important conclusion from Eq. (III.13) is that the coupler angle $\beta = 45°$ is a unique angle because both k_{ry0} and k_{rz0} are a function of 2β. From another perspective, $\beta = 45°$ symmetrically rotates the incoming light, reserving the etendue. Any other coupler angles lead to an unsymmetrical reflection profile and thus increase etendue. Furthermore, such unsymmetrical reflections result in larger reflection angles, requiring a larger waveguide numerical aperture (NA) to confine light, as illustrated in Figure 14. Consequently a coupler angle $\beta = 45°$ is always desired.

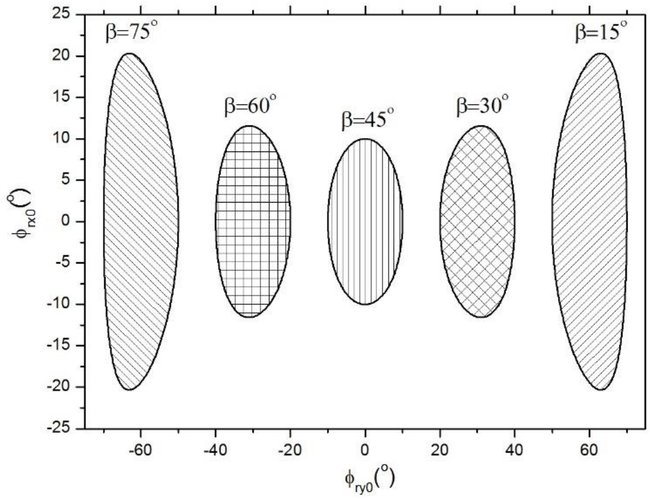

Figure 14. Plot of reflection angles for different coupler angles β in waveguide XZ plane $\phi_{rx0} = \arctan\left(k_{rx0} / k_{rz0}\right)$ and YZ plane $\phi_{ry0} = \arctan\left(k_{ry0} / k_{rz0}\right)$ when $\gamma = 10°$.

Besides the above discussion of coupler angle, $\beta = 45°$ determines the waveguide thickness t. Assuming the spot size change from refractions at air/cladding/waveguide interfaces is negligible, the minimum thickness $t_{\min} = d$, where d can be calculated from Eq. (III.6). As a result, substituting t in Eq. (III.2) using $t_{\min}$, the maximum concentration from the structure is

$$C_{1\max} = \frac{D^2}{d \times t_{\min}} = \frac{D^2}{d^2} = \frac{4}{\pi} C_{lens}. \qquad \text{(III.17)}$$

Unlike Karp’s design mentioned in II.2 where the waveguide thickness cannot be reduced due to decoupling loss, this lens-waveguide system preserves the lens concentration ability and always achieves higher concentration ratio.

III.2.3 Waveguides

The main loss mechanism for waveguides is the propagation loss except for TIR conditions given in Eqs. (3.14)~(3.16). Again, trace a beam of light (θ,Ω) after a particular lens P as shown in Figure 15, where $1 \le P \le N$. The reflected light travels $\left[(P-1)+\frac{1}{2}\right]D\times\cos\Theta$ along the z axis. The distance traveled inside the waveguide for light (θ,Ω) is

$$L_P(\theta,\Omega,P)=\frac{\left[(P-1)+\frac{1}{2}\right]D\times\cos\Theta}{k_{rz0}}. \tag{III.18}$$

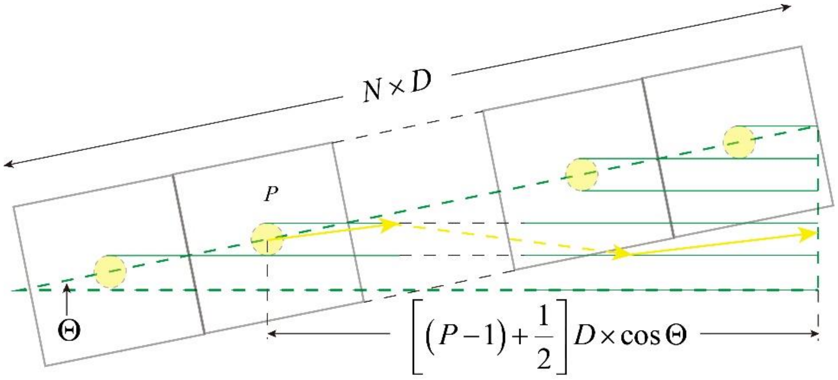

Figure 15. Calculation of propagation loss.

The total propagation loss is estimated as the exponential decay of the distance L_P multiplied by the waveguide material absorption coefficient $\alpha(\lambda)$ with the mean of all lenses P,

$$\eta_{sp}(\lambda) = \left\langle \sum_{P} \int_{0}^{\theta_M} \int_{0}^{2\pi} \exp(-\alpha L_P)\, d\Omega d\theta \right\rangle. \tag{III.19}$$

The propagation loss is a weak function of wavelength due to the wavelength dependence of the absorption coefficient. It is desirable to use transparent materials (in terms of the interested solar spectrum) for both minimizing absorption and spectrum distortion.

III.3 Parameter tradeoffs and simulation results for an exemplar system

Using the equations in section III.2, the optical efficiency η is the product of

- Coupling loss η_c calculated from Eq. (III.12);
- Waveguide propagation loss η_{sp} from Eqs. (III.14)~(III.16) and Eq. (III.19);
- Fresnel reflection loss $\eta_{Fresnel}$.

Any loss in the lens array is omitted. Clearly, the total efficiency η is a function of the maximum incident field δ_M, f-number of the lens array, material refractive indices, and waveguide/lens array dimensions. Note that when proper materials are selected, propagation loss is usually negligible comparing to other loss mechanisms.

As an example, concentration C_1 as well as optical efficiency η is simulated in Matlab using different incident angles δ_M, f-numbers $f/\#$, and waveguide refractive indices n_w. No dispersion is considered by setting wavelength $\lambda = 0.5876\mu m$. The waveguide absorption coefficient is assumed to be $\alpha \sim 7\times10^{-4}/cm$. The cladding, substrate and receiver are all set to be air ($n_s = n_c = n_r = 1$). Each of the lenses is $1cm\times1cm$. Fresnel reflection loss is intentionally neglected in this simulation.

Figure 16 shows the simulation results with f-number as the abscissa, concentration as the left y axis and efficiency as the right y axis. Concentration depends only on the $f/\#$ and δ_M combinations as in Eqs. (III.7) and (III.17). Setting the design goal for concentration and either the angular acceptance or lens f-number, the other parameter can be calculated. Achieving $C > 500$ concentration is not easy, though, and it becomes impossible for $\delta_M > 1^\circ$. It is almost not feasible if the goal is set as $C = 1000$ even under this ideal situation. As stated before, this results from the fact that a lens array is not an ideal concentrator. Hence a secondary concentrator further increases concentration can be used. Detailed discussions can be found in III.4.

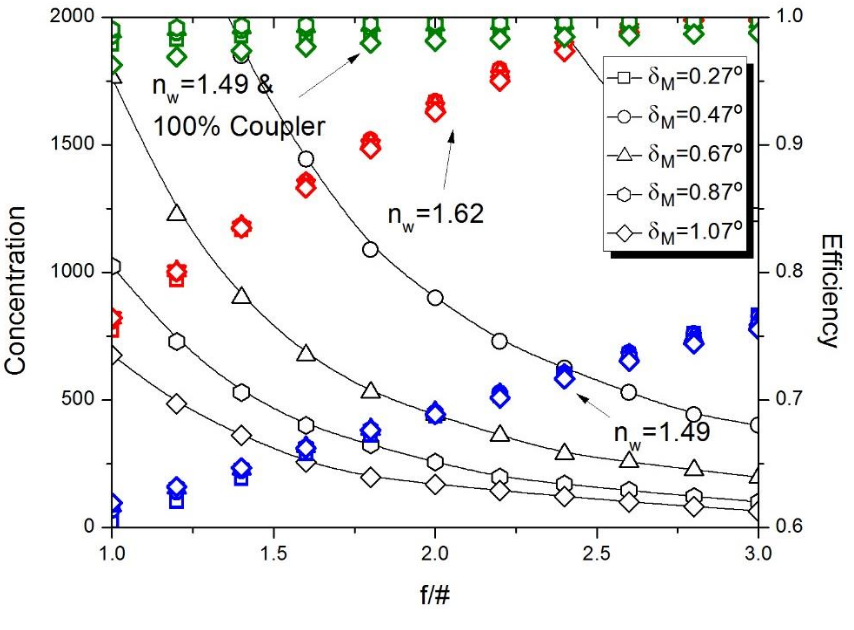

Figure 16. Plot of concentration and optical efficiency in terms of different f-number, incident field and waveguide material combinations.

Clearly, optical efficiency is limited by the coupler surface and f-number is the dominating factor comparing to incident field, as indicated in Eq. (III.8). When f-number goes down, edge ray angles become so large that TIR condition is easily violated in the coupler interface. The critical angle for a $n_w = 1.62$/air interface is $38.1°$. Due to the existence of 45° coupler, $\gamma_M < 6.9°$ is required which corresponds to $f/2.5$ if δ_M is set 0, matching well with the dropping point for $n_w = 1.62$ in Figure 16. This f-number goes up to $f/6.7$ for $n_w = 1.49$. Hence a metallic reflecting coating at the coupler surface is always needed for smaller refractive indices and the only loss becomes propagation loss. It is worth mentioning that Figure 16 shows the ideal case and in reality a reflective coating does not have 100% reflectance.

In this particular simulation, light is made sure in guided mode when traveling inside waveguides since the waveguide is surrounded by air. If a substrate or cladding is used, for example $n_s = 1.45$, the critical angle in y axis becomes $\phi_{c-c/s} = 76.7°$ for $n_w = 1.49$, which requires $\gamma_M < 90° - \phi_{c-c/s} = 13.3°$ for the light after the lens array; this approximately corresponds to $f/\# > 1.37$ by setting $\delta_M = 0$ in Eq. (III.8). Again, even in this extreme example, the limiting factor is still the coupler TIR surface.

In summary, concentration is determined by the combination of maximum incident angle δ_M and lens f-number. Smaller δ_M and f-number lead to higher concentration in trade of precise tracking requirement and light decoupling. Optical efficiency mainly depends on TIR at the coupler interface. With small lens f-numbers, large edge ray angles may exceed the critical angle and light will be decoupled. As a result, proper δ_M and lens f-number are chosen according to waveguide materials. Metallic reflective coating may be needed for low refractive index materials.

III.4 A tapered waveguide as a secondary concentrator

As stated in previous sections, lenses are the only concentrator in this setup. Considering lenses are not ideal, it is desirable to connect the structure to a secondary concentrator. A secondary concentrator not only increases concentration, but also alleviates constrains of the waveguide materials and lens f-numbers discussed in III.3. An x axis tapered waveguide is selected as the secondary concentrator connected directly to the end of the primary structure (Figure 17). Such a structure, comparing with other setups, e.g. a CPC used in [33], is easy to design and realize. The tapered waveguide can be viewed as a near-ideal concentrator as discussed below.

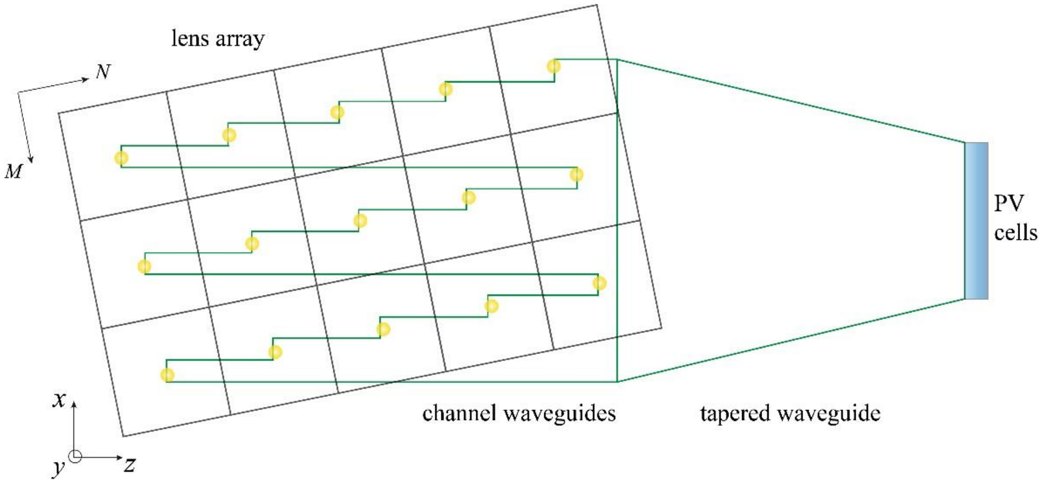

Figure 17. An x axis tapered waveguide is connected to the end of the primary structure as a secondary concentrator. It provides C_2 more concentration.

Figure 18 shows the important parameters associate with a tapered waveguide. Since a waveguide concentrator is a 2D design, the thickness t remains the same as the primary part. The initial width, in order to connected with the channel waveguides, is $WT_0 = M \times N \times W$. If the tapered angle is ξ and the waveguide length is L, the output side of the waveguide is $WT_1 = WT_0 - 2L\tan\xi$. As a result, the secondary concentration brought by this tapered waveguide is

$$C_2 = \frac{WT_0}{WT_1} = \frac{1}{1 - 2 \times \frac{L}{WT_0} \times \tan\xi} \triangleq \frac{1}{1 - 2L_N \tan\xi}. \tag{III.20}$$

$L_N = L / WT_0$ is designated as normalized tapered waveguide length. The total system concentration is therefore

$$C = C_1 \times C_2, \tag{III.21}$$

where C_1 and C_2 are defined in Eqs. (III.2) and (III.20), respectively.

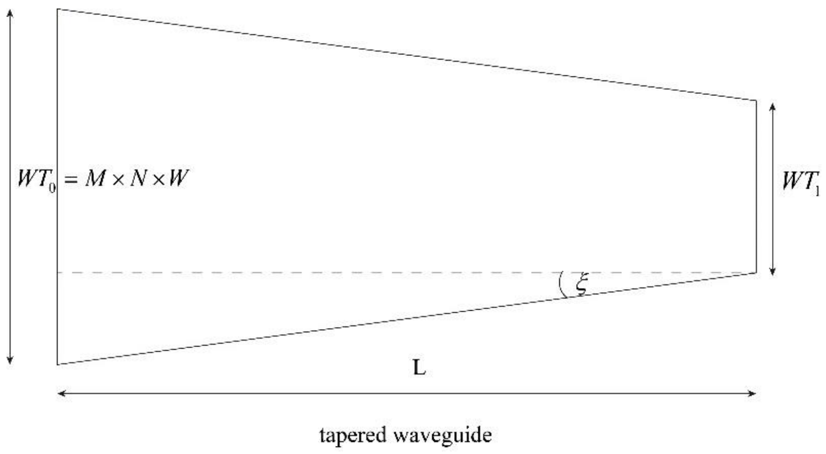

Figure 18. Parameters associated with the tapered waveguide part.

After entering the tapered waveguide, light $\overrightarrow{k_r} = \left(k_{rx0}, k_{ry0}, k_{rz0}\right)$ gains 2ξ for its propagation angle in XZ plane every time it hits the sidewalls, while the reflection angle remains the same along y axis. In other words, light angular space becomes larger in XZ plane the as additional concentration is achieved. Therefore light travels more distance than that in straight waveguides. Each reflection is viewed as an image of the waveguide by its own sidewall, as shown in Figure 19. Using the law of cosines (R , r and propagation path forms a propagation triangle), the distance L_{TXZ} the light travels in the XZ plane can be expressed as $r^2 = R^2 + L_{TXZ}^2 - 2RL_{TXZ}\cos\left(\phi_{rx0} - \xi\right)$, where $R = \frac{WT_0}{2\sin\xi}$,

$r = R - \frac{L}{\cos\xi}$ are radius of the circles and $\phi_{rx0} = \arctan\frac{k_{rx0}}{k_{rz0}}$ is the initial reflection angle in X-Z plane. Solve the equation for L_{TXZ} ,

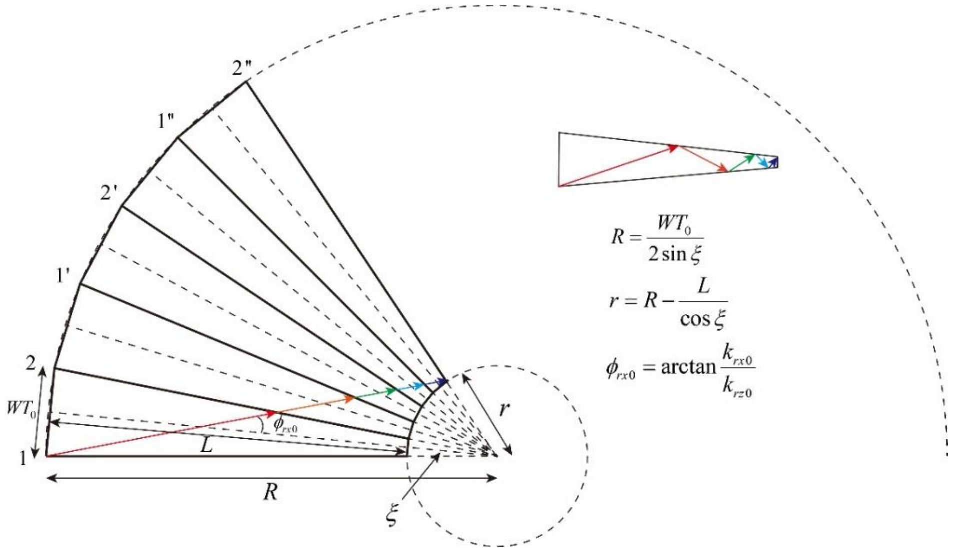

Figure 19. The propagation of light inside the tapered waveguide can be viewed as the waveguide imaged by its sidewalls. Inset is the real propagation path.

$$L_{TXZ}\left(\theta,\Omega\right)=WT_0\times\frac{\cos\left(\phi_{rx0}-\xi\right)-\sqrt{\cos^2\left(\phi_{rx0}-\xi\right)-4L_N\tan\xi+4L_N^2\tan^2\xi}}{2\sin\xi}. \quad \text{(III.22)}$$

The total distance L_T is

$$L_T\left(\theta,\Omega\right)=\frac{L_{TXZ}}{\sqrt{k_{rx0}^2+k_{rz0}^2}}=WT_0\times\frac{\cos\left(\phi_{rx0}-\xi\right)-\sqrt{\cos^2\left(\phi_{rx0}-\xi\right)-4L_N\tan\xi+4L_N^2\tan^2\xi}}{2\sin\xi\sqrt{k_{rx0}^2+k_{rz0}^2}}. \quad \text{(III.23)}$$

Again, the total propagation loss is estimated as the exponential decay of the distance L_T multiplied by the waveguide material absorption coefficient $\alpha\left(\lambda\right)$,

$$\eta_{tp}\left(\lambda\right)=\int_0^{\theta_M}\int_0^{2\pi}\exp\left(-\alpha L_T\right)d\Omega d\theta. \quad \text{(III.24)}$$

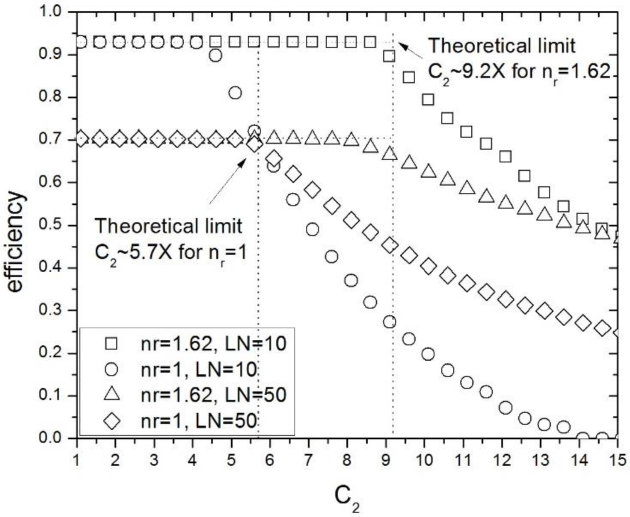

Figure 20. The performance of tapered waveguide concentrator for different parameters. Theoretical limits are calculated based on $C_{2\lim}=\frac{n_r}{n_w\sin\phi_{rx0}}$.

In order to explore the concentration performance of a tapered waveguide, an efficiency plot based on a given f-number ($f/3$) and a maximum incident angle ($\delta_M = 0.7°$) is shown in Figure 20 using different combinations of receiver refractive indices n_r and normalized waveguide length L_N. The refractive index of waveguide is $n_w = 1.62$ and $M = 10$. It turns out that the absolute efficiency depends on L_N because propagation loss in the tapered waveguide begins to be the main factor. On the other hand, the dropping point is determined by the refractive index of the receiver space, which approaches to the 2D etendue limit in each case, as indicated by Figure 20. There are two factors that limit the maximum concentration, i.e. 1. sidewall TIRs in Eq. (III.14); and 2. waveguide/receiver TIRs in Eq. (III.16), as illustrated in Figure 21. In case 1, still using the propagation triangle in Figure 19, the maximum waveguide concentration would be achieved when the output light angle is the critical angle $\phi_{c-sw} = \arcsin \frac{n_r}{n_w}$,

$$\frac{\sin\left(90° + \phi_{c-sw}\right)}{R} = \frac{\sin\left(\phi_{rx0} - \xi\right)}{r}. \qquad \text{(III.25)}$$

Therefore,

$$C_{2\max} = \frac{R}{r} = \frac{\cos\phi_{c-sw}}{\sin\left(\phi_{rx0} - \xi\right)} \approx \frac{\cos\phi_{c-sw}}{\sin\phi_{rx0}} = \frac{n_r \frac{n_w}{n_r}\cos\phi_{c-sw}}{n_w \sin\phi_{rx0}}. \qquad \text{(III.26)}$$

Eq. (III.26) indicates that when sidewall TIR is the limiting factor, the maximum waveguide concentration can achieve $\frac{n_w}{n_r}\cos\phi_{c-sw}$ times the theoretical limit. For example, when $n_w = n_r = 1.62$, $\frac{n_w}{n_r}\cos\phi_{c-sw} = 0.78$, which is about 80% of the etendue limit, as marked for $n_r = 1.62$ in Figure 20.

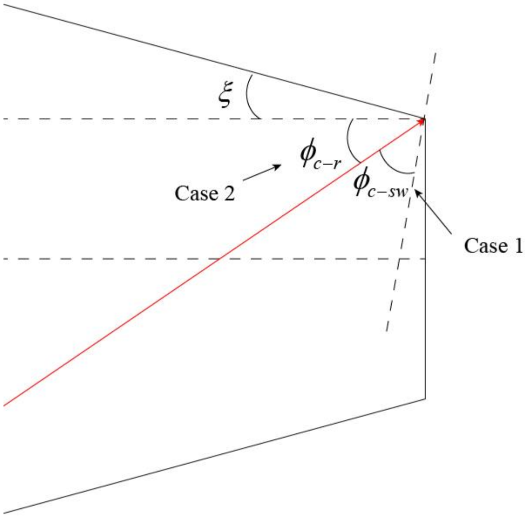

Figure 21. Illustration of the two limiting factors for maximum waveguide concentration.

On the other hand, if the waveguide/receiver interface is the limiting factor, Eq. (III.25) is modified by replacing $90° + \phi_{c-sw}$ with $180° - \xi - \phi_{c-r} = 180° - \xi - \arcsin\frac{n_r}{n_w}$,

$$C_{2\max} = \frac{\sin\left(\phi_{c-r} + \xi\right)}{\sin\left(\phi_{rx0} - \xi\right)} \approx \frac{\sin\phi_{c-r}}{\sin\phi_{rx0}} = \frac{n_r}{n_w \sin\phi_{rx0}}. \qquad \text{(III.27)}$$

Eq. (III.27) is the same expression with that of an ideal 2D concentrator. In case 2, however, vector k_y also plays a role in determining the critical angle because the 2D XZ plane in Figure 21 does not show the maximum output angle. In fact, the output angle is given by

$$\phi_{c-r} = \arccos k_z = \arccos \sqrt{\frac{1-k_y^2}{1+\tan^2 \phi_{c-r2D}}}. \qquad \text{(III.28)}$$

Fortunately k_y^2 is usually a small number and $\phi_{c-r} = \phi_{c-r2D}$ is a good approximation. Nevertheless, whichever case the tapered waveguide is under, its performance approaches to that of an ideal 2D concentrator. Hence the tapered waveguide can be viewed as a near-ideal 2D concentrator.

Combining both the primary and secondary concentrators, Figure 22 shows a plot of $C_{geo} = 800$ concentrator under different f-number and δ_M combinations (C_1). Parameters remain the same with those in Figure 16, i.e. the waveguide refractive index is $n_w = 1.62$, the absorption coefficient is $\alpha \sim 7\times10^{-4} / cm$, the cladding and the substrate are both air ($n_s = n_c = 1$), the lens is $1cm \times 1cm$, $M = 10$, the normalized tapered waveguide length is $L_N = 10$ and Fresnel reflection loss is neglected. The blue data points represent an index-matching receiver space while the red ones are air. Any other receiver space would lie between these two extreme cases.

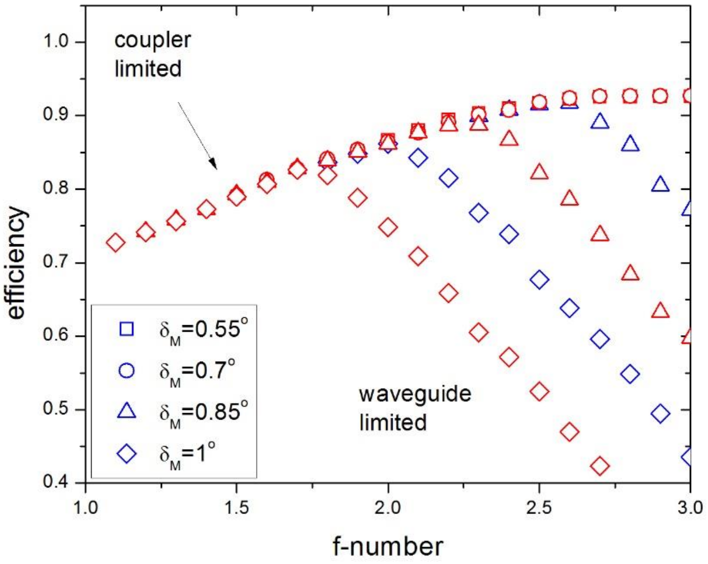

Figure 22. Efficiency plot by combining primary and secondary concentrators for different f-numbers and maximum incident angles.

It is easily seen that each curve can be divided into two parts, regardless of the receiver refractive index, with the turning point to be the maximum achievable efficiency, which means that for every designed maximum incident field, there exists an optimal f-number that maximizes the efficiency. The left portion of the curves is designated as coupler limited region, where the efficiency is mainly determined by the TIR loss at the coupler interface due to smaller f-numbers. Since concentration from the lenses are large enough in these scenarios, secondary concentrators usually lie in ideal regions that has only propagation loss. The efficiency increases with f-numbers because the edge ray angles become smaller. If the TIR coupler surface is replaced with a metallic coating, the coupler limited region would be flat and remain at a single efficiency that is determined by the reflectance of the reflective coating. The right portion of the decreasing efficiency, in contrast, is determined by the tapered waveguide concentration ability. Since larger f-numbers bring smaller edge ray angles as well as smaller concentration, it requires more concentration from the tapered waveguide. When it reaches the maximum waveguide concentration, the efficiency begins to drop. As the tapered waveguide performance is related to the receiver space, smaller receiver refractive index leads to drops at smaller f-numbers. For each waveguide material n_w and designed concentration C, a plot like Figure 22 can be made and the optimal operating condition can be determined from the figure. It is worth noting that comparing to Figure 16, the secondary concentrator relieves the requirements for the lens array under high concentrations. $C_{geo} = 800$ can be easily achieved with relatively high efficiency even under large incident angles.

Using Eqs. (III.7), (III.8), (III.17) and (III.27), the maximum achievable concentration of the proposed waveguide concentrator can be estimated under ideal situations,

$$C_{1\max} = \frac{\pi}{4} C_{lens} = \frac{1}{4\left(f/\#\right)^2 \tan^2 \delta_M}, \tag{III.29}$$

$$C_{2\max} = \frac{n_r}{n_w \sin\phi_{rx0}} = \frac{n_r}{\sin\left[\arctan\left(\tan\delta_M + \dfrac{1}{2f/\#}\right)\right]}, \text{ and} \tag{III.30}$$

$$C_{\max} = C_{1\max} \times C_{2\max}. \tag{III.31}$$

The theoretical maximum concentration $C_{\max}$ is therefore determined only by the lens f-numbers, the designed maximum incident angle and the receiver refractive index. An exemplar plot by setting $n_r = 1$ is shown in Figure 23. The shaded region in the plot marks impossible combinations of f-numbers and incident angles that can achieve $C_{geo} = 1000$. Note, though, Figure 23 is an ideal plot without considering any lens aberrations and the small f-number region will be limited by the TIR conditions at the coupler interface if no reflective coatings are used as discussed before. The upper efficiency limit of a real system also depends on coupling loss, Fresnel reflections and material absorptions.

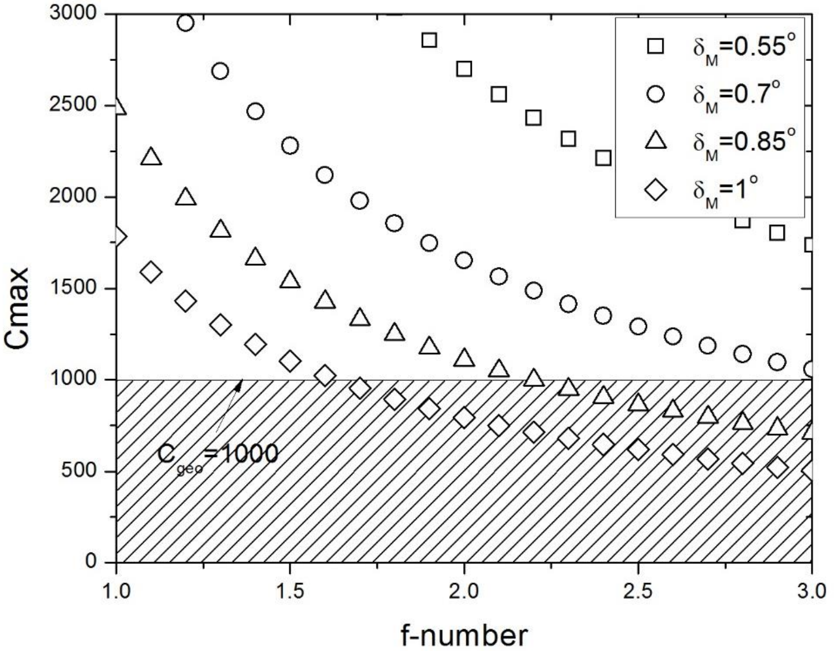

Figure 23. Estimated theoretical maximum concentration ($n_r = 1$).

III.5 A ZEMAX model

ZEMAX is a popular ray tracing program developed by an American company Radiant ZEMAX. In order to examine the practical performance of the proposed structure, ZEMAX EE non-sequential mode is used to model the entire setup.

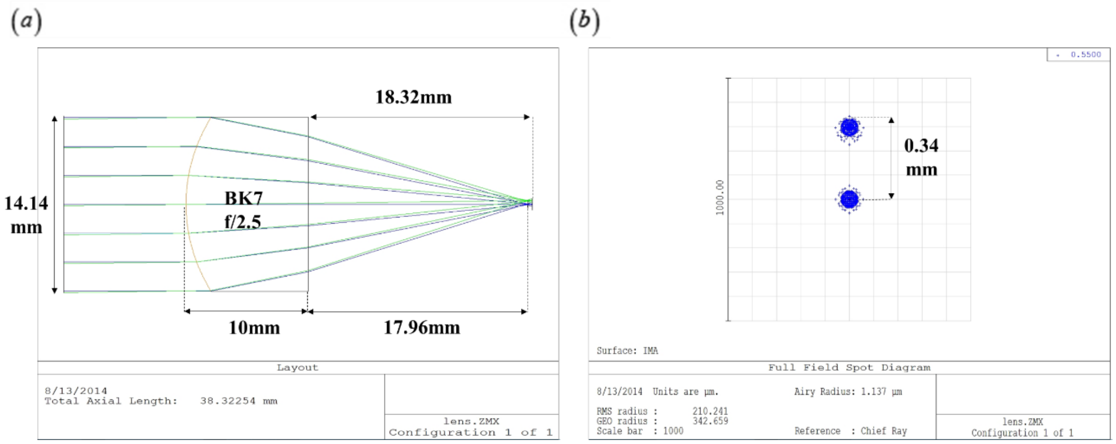

Figure 24. (a) Lens dimensions and properties and (b) its spot diagram.

In a preliminary model, an ideal blackbody source from 400nm to 1600nm at 5777K with ±0.7° incidence angle is set as the light source to simulate the incoming useful sunlight as well as the maximum incident angle. Figure 24 shows the lens properties used in simulation. The f-number of the $1cm \times 1cm$ square lens array is $f/2.5$ as defined in previous sections. The lens array is made of BK7 glass and the conic constant is optimized to yield minimum spot size. Below the $9 \times 12\,(M \times N)$ lens array, a total of 108 channel waveguides are placed side by side and are tilted according to the calculations in III.1. These waveguides use Schott F2 glass. The cross section of each waveguide is $0.083cm \times 0.083cm$. The normalized length of the tapered structure is $L_N = 10$. The output surface area is $0.083cm \times 1.62cm$. Therefore $C_{geo} = 803.2$ with $C_1 = 145$ and $C_2 = 5.53$. A summary of some of the most important component properties is shown in Table 2. Figure 25(a) shows a top view of the primary concentrator, while Figure 25(b) proves that the output light intensity is evenly distributed at the end of the waveguide. Several detectors are placed in the setup to measure the efficiency at different locations. Detector #1 is placed right after the back surface of the lens array; detector #2 is placed below the waveguide top surface; detector #3 is set before light entering the tapered waveguide to check the efficiency of the primary concentrator; there are also two detectors #4 and #5 before and after the tapered waveguide end. Locations of detectors #1~#3 are illustrated in Figure 26.

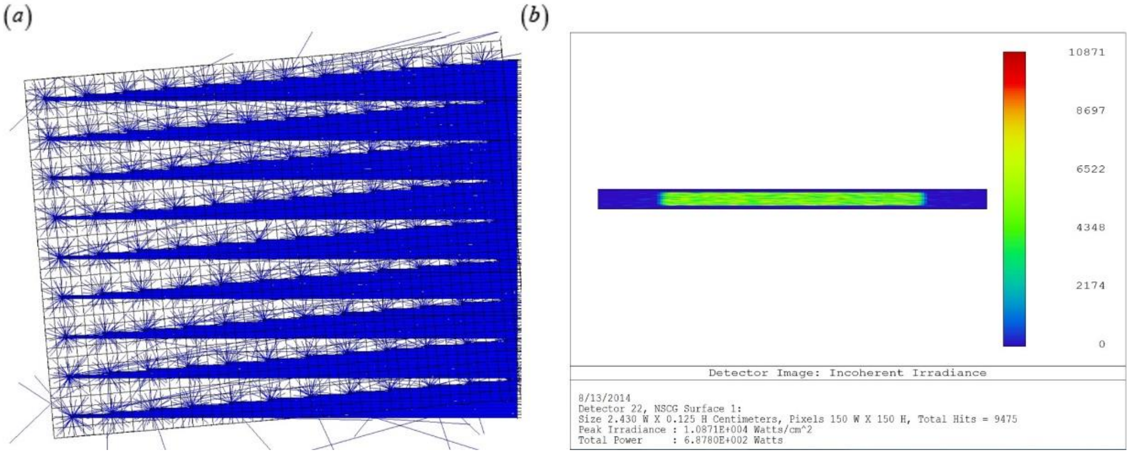

```
8/13/2014
Detector 22, NSCG Surface 1:
Size 2.430 W X 0.125 H Centimeters, Pixels 150 W X 150 H, Total Hits = 9475
Peak Irradiance : 1.0871E+004 Watts/cm^2
Total Power     : 6.8780E+002 Watts
```

Figure 25. (a) Drawing from ZEMAX of part of the setup; and (b) the uniform output.

Table 2. A summary of components used in a preliminary model in ZEMAX

Object	Comment	Parameters							
Source Two Angle	Light source	Tilt about z 4.78	Power 1000	X half width 4.5	Y half width 6	X half angle 0.7	Y half angle 0.7	-	-
Lenslet Array	Square lens array	Material BK7	Thickness 1	X half width 0.5	Y half width 0.5	Radius -1.29153	Conic -0.41565	Number in X 9	Number in Y 12
Rectangular Volume	Parent of array object	Material F2	Length 12	X half width 0.04167	Y half width 0.04167	Front Y angle 45	-	-	-
Array	First array of parent object	X position -0.45551	Y position 2.84768	Z position -5.48092	Number Z’ 12	Z’-X 0.08283	Z’-Z 0.99426	-	-
Array	Array of parent object (Ref #.4)	X position 0.99426	Y position 0	Z position -0.08283	-	-	-	-	-
Rectangular Volume	Tapered Waveguide	Material F2	Y position 2.84768	X1 half width 4.5	Y1 half width 0.04167	X2 half width 0.81	Y2 half width 0.04167	Z length 90	-

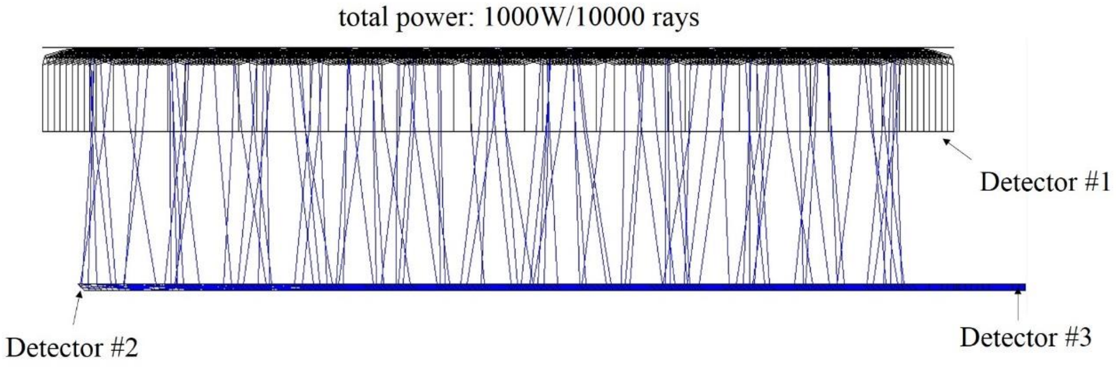

Figure 26. Illustration of detector locations.

Table 3 lists an efficiency breakdown. 10000 rays with 1000W power are lunched and monitored by the detectors. Structural losses, including TIR loss at the coupler interface (98.6%), coupling loss at the coupler (97.8%), decoupling loss from the tapered waveguides (98.8%) and TIRs at the waveguide end (86.4%) described by Eq. (III.16), are about 82.3% of the total loss. If an index matching receiver is used, this loss would reduce to 95.3%. TIR loss at the coupler interface mainly results from large incident angles due to the small f-number; coupling loss results from aberrations of the lens array. Since only first-order properties are used when modelling the lens array, the real spot size is actually larger than the calculations from the math model and chromatic aberration also plays a role in increasing the spot size. Hence part of the light leaks from the coupler surface. When the tapered waveguide exceeds its concentration upper limit, light begins leaking from the sidewalls, leading to decoupling loss. Other than the above structural losses, it turns out Fresnel reflections on multiple interfaces are a big factor, accounting for only 79.9% transmission due to Fresnel reflections. Light propagation loss in the tapered waveguide is 86.9% because of the $90cm$ waveguide length. It can be further reduced using smaller lens/waveguide dimensions.

Table 3. Efficiency breakdown for the initial setup.

Detector #	Rays	Power (W)	Efficiency
1	10000	916.38	Fresnel 91.6%
2	10000	865.81	Fresnel 94.5%
3	9638	826.13	Spot size 97.8% TIR 98.6% Propagation 99.0%
4	9523	709.98	Decoupling 98.8% Propagation 86.9%
5	8226	566.13	TIR 86.4% Fresnel 92.3%
			Total structural 82.3% **Total** 56.6%

In order to increase the overall efficiency, several modifications are made to this initial setup. First of all, an index matching receiver space is assumed so that both Fresnel reflections and TIRs at the waveguide end can be eliminated. Secondly, a layer of MgF_2 anti-reflection coating (AR coating) is deposited on both sides of the lens array to reduce Fresnel reflections. A new efficiency breakdown is shown in Table 4. Fresnel loss is minimized with the use of AR coatings on lens surface. Again, it is desirable to decrease the system dimension for lower propagation loss.

Table 4. Efficiency breakdown for the modified setup.

Detector #	Rays	Power (W)	Efficiency
1	10000	959.27	Fresnel 95.9%
2	10000	906.29	Fresnel 94.5%
3	9634	864.44	Spot size 97.8% TIR 98.6% Propagation 99.0%
4	9503	743.93	Decoupling 98.6% Propagation 87.2%
			Total structural 95.0% **Total** 74.4%

CHAPTER IV

STRUCTURE OPTIMIZATIONS AND DISCUSSIONS

Discussions in this chapter can be divided into three parts. First of all, a Fresnel lens design optimized based on solar spectrum is used to replace the conventional lens array. A Fresnel lens is inherently an aspherical surface which minimizes spherical aberrations under small f-numbers. Hence it shows superior performance in solar concentrators comparing to a conventional spherical surface. Secondly a new secondary concentrator design is proposed instead of using a tapered waveguide previously discussed in III.4. As the primary concentration ratio of the basic concentrator structure depends only on the lens array, considering chromatic aberrations as a result of the broad solar spectrum, it is almost impossible to achieve $C_{geo} > 300$ from a single layer of lens array. However, the tapered waveguide secondary concentrator consumes space without actively collecting sunlight. It is therefore necessary to explore the possibility of increasing structure concentration without separate secondary optics while maintaining the lossless light propagation mechanism. As result, an integrated secondary concentrator is designed. Finally, we extend the concentration in the structure to 3D, which maximizes concentration up to $C_{geo} = 1000$ while keeps low propagation loss. These optimizations are important steps towards the realization of the basic structure for practical uses.

IV.1 The Fresnel lens array

IV.1.1 Conventional lens designs

Spherical and aspherical surfaces used in a plano-convex lens are compared in ZEMAX. A more complete light source is modeled to represent sunlight using light two angle light source type in ZEMAX (comparing to that in III.5). The source object is configured as:

- Uniform irradiance of $855W/m^2$ on the top surface of the lens array;
- Extending an angle of $0.266°$;
- Wavelength from 350nm~1750nm weighted by AM 1.5D, $\Delta\lambda = 10nm$.

A detector view of the modeled sunlight is shown in Figure 27.

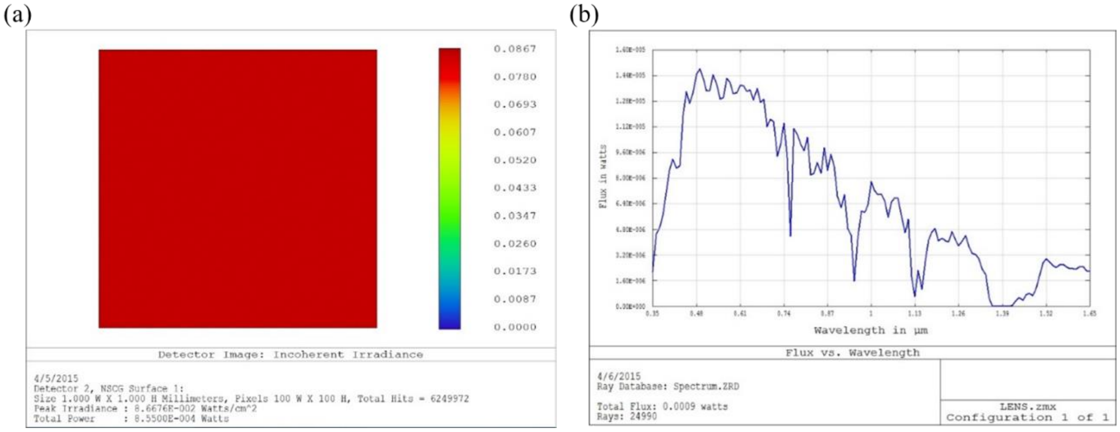

```
4/5/2015
Detector 2, NSCG Surface 1:
Size 1.000 W X 1.000 H Millimeters, Pixels 100 W X 100 H, Total Hits = 6249972
Peak Irradiance : 8.6676E-002 Watts/cm^2
Total Power     : 8.5500E-004 Watts
```

```
4/6/2015
Ray Database: Spectrum.ZRD

Total Flux: 0.0009 watts
Rays: 24990
```

Figure 27. Detector views of (a) the uniform irradiance on the top surface of the lens array and (b) the spectrum.

BK7 is used as a common glass material. The detector plane is an $1mm \times 1mm$ square, which is placed at a distance of 25mm from the top lens surface (which resembles a typical value of the focal length). At each given lens diameter D, the lens thickness t, radius of curvature R and conic constant K (if aspherical) are optimized automatically in ZEMAX to give maximum flux on the detector plane. Normal incidence is used and no Fresnel reflections or absorptions are considered in the optimization process. The acceptance angle (defined as the point where the efficiency drops to 90% in this chapter) is then determined by tilting the source at different angles.

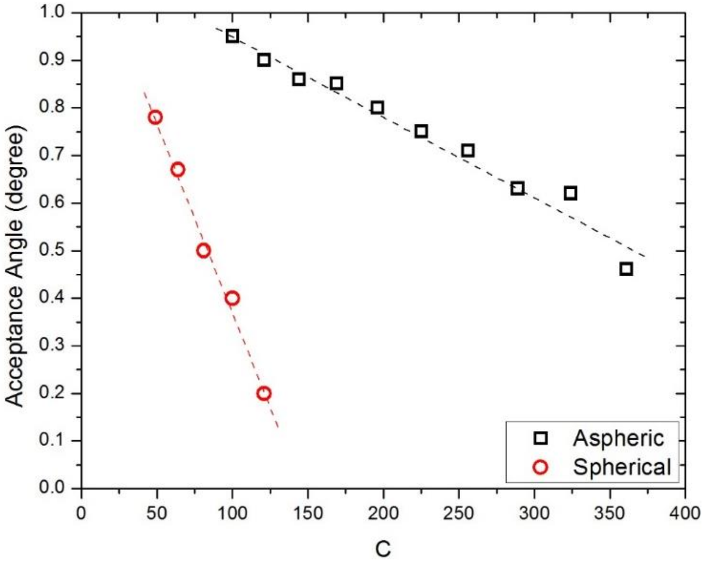

Figure 28. Acceptance angle comparison between a spherical and an aspherical lens.

In all concentrations (diameters), the aspherical surface outperforms its spherical counterpart (Figure 28), mainly by reducing spherical aberrations. As concentration decreases, their difference is reduced and the leading aberration becomes chromatic aberration from the broadband solar spectrum. A typical plot of aspherical lens acceptance angles and its comparison to a spherical lens at $C_{geo} = 100$ are shown in Figure 29.

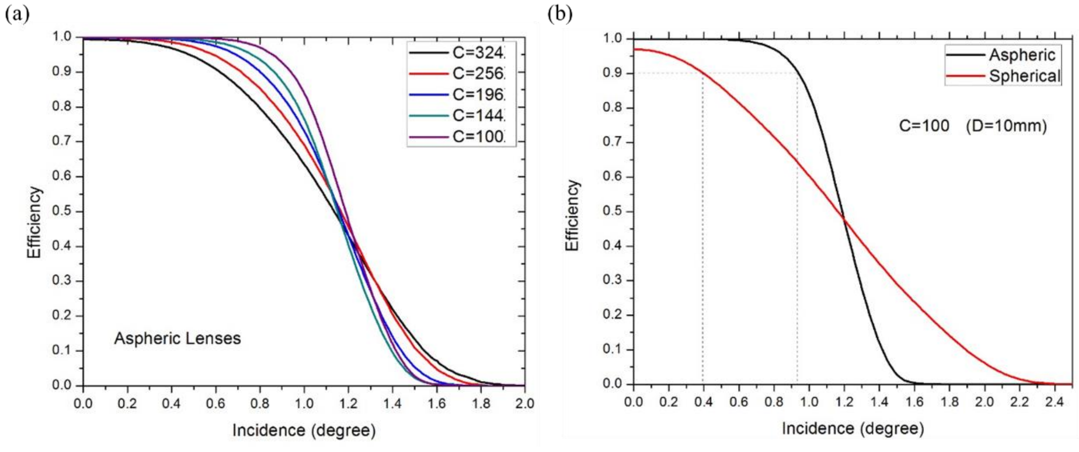

Figure 29. (a) Aspherical lenses at different concentration and (b) comparison between an aspherical and a spherical surface at 100 geometric concentration.

While the best a spherical lens can concentrate is around $C_{geo} = 100$ with $\pm 0.4°$ angular acceptance, an aspherical reaches around $C_{geo} = 350$ with $\pm 0.45°$ angular acceptance, which is necessary if high concentration is desired.

IV.1.2 A Fresnel lens optimized for solar spectrum

A Fresnel lens is inherently an aspherical surface due to the individually controlled prism angles. Conventionally the simplest design aims at a single wavelength as described in I.3.3.2, it still suffers chromatic aberration as in the case of an aspherical surface. Watson and Jayroe [35] proposed a Fresnel lens design based on geometric optics and solar spectrum (blackbody radiation is assumed). We adopt the idea of Circle of Least Confusion (CLC) from broadband light source in their design as illustrated in Figure 30. The longest wavelength (represented by θ_{fR}) and the shortest (θ_{fB}) are focused at different focal points due to their refractive index difference in the lens material (n_R and n_B). CLC is defined as the intersection of the focusing rays at the longest and the shortest wavelengths and its distance from the Fresnel surface f can be calculated by

$$\tan\theta_{fR} = \frac{2r}{f} - \tan\theta_{fB}, \tag{IV.1}$$

$$\theta_{fR} = \arcsin\left\{ n_R \sin\left[\theta_{BL} - \arcsin\left(\frac{\sin\theta_s}{n_R} \right) \right] \right\} - \theta_{BL,} \text{ and} \tag{IV.2}$$

$$\theta_{fB} = \arcsin\left\{ n_B \sin\left[\theta_{BL} - \arcsin\left(\frac{\sin\theta_s}{n_B} \right) \right] \right\} - \theta_{BL}. \tag{IV.3}$$

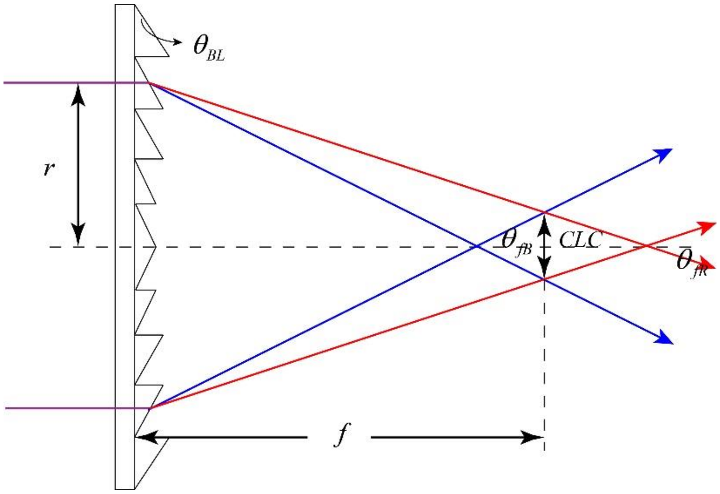

Figure 30. Circle of Least Confusion (CLC).

$\theta_s = 0.266°$ is the solar half angle; θ_{BL} and r are the prism blazing angle and its distance from the lens center, respectively. r is set as the sum of each individual prism w_i (pitch) $r = \sum x_i$, θ_{BL} for a particular prism i can be obtained from Eqs.

(IV.1)~(IV.3). In the realization of this design, θ_{BL} is calculated from Newton's method [36] and TIR is checked at each prism surface. TIR at large θ_{BL}s limits the maximum lens diameter and hence the maximum concentration.

The optimum lens diameter is finally determined by angular acceptance and concentration requirements. Higher concentration (large lens diameter) brings larger CLC spot size and hence smaller angular acceptance. Figure 31(a) shows a typical lens (material: PMMA) efficiency plot over incident angle at $Pitch = 200\mu m$, $D = 14.04mm$ and $f = 20mm$ ($C_{geo} = 197$, $f/1.42$), where only structural loss is considered while Fresnel reflections, material absorptions etc. are neglected. Figure 31(b) is the comparison between a Fresnel lens and an aspherical lens. The aspherics are better at smaller concentrations while the Fresnels are better at large concentrations, which may be due to the extremely curved surface of the aspherics at large concentrations. The diameter is so large that the lens becomes thick and almost an entire half circle is needed to form the aperture, leading to degraded performance. Fresnel lenses are apparently a better choice where $C_{1geo} > 200$.

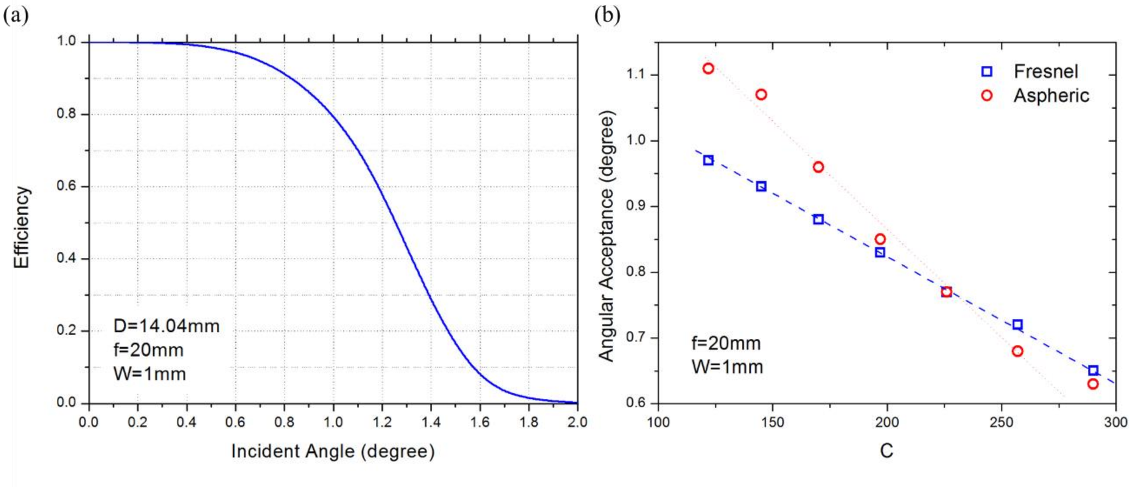

Figure 31. (a) A typical Fresnel lens efficiency plot. (b) Angular acceptance comparisons between a Fresnel lens and an aspherical lens for different concentrations (lens diameters).

We also simulate the manufacturing process by introducing a $\beta = 3^\circ$ draft angle at the vertical walls (inset of Figure 32). The result is shown in Figure 32. The maximum efficiency drops to 97.4% compared to the ideal case. Other manufacturing defects, e.g. rounding, may also exist and can be modeled using numerical methods [37].

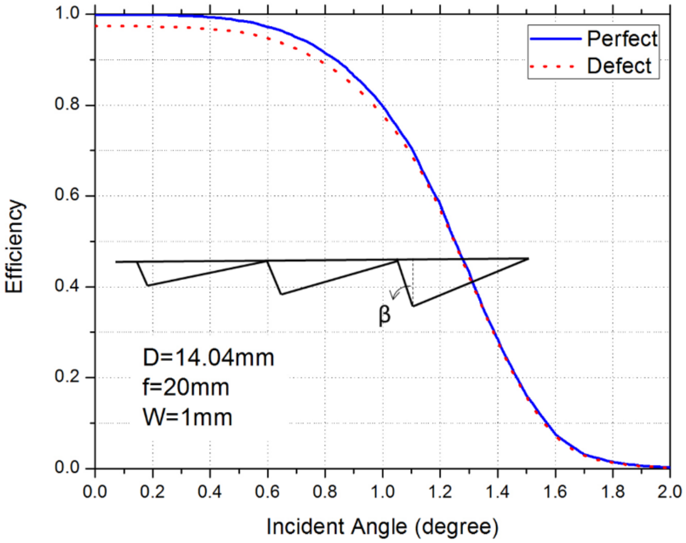

Figure 32. Simulation of lens performance with $\beta = 3°$ draft angle. Inset illustrates the definition of draft angle.

IV.2 An integrated secondary concentrator design

IV.2.1 Motivation and introduction

The primary concentration ratio of the structure depends only on the lens array. Previously in III.4, a separated tapered waveguide is used as a secondary concentrator. However, this separated waveguide consumes space without collecting sunlight and therefore reduces the percentage of active area. An alternative that integrates the tapered waveguide part into the sunlight collection area is designed and simulated to circumvent the problem.

Referring to Eqs. (III.3) and (III.4) and Figure 10, the number of lenses in a row $N = N_0$ is limited by $N_0 = \sqrt{\frac{D^2}{W^2} - 1}$, where D is the lens diameter and W is the width of the waveguide. Adding any more lenses along N without modifying the waveguide is impossible; waveguides begin to overlap with their neighbors.

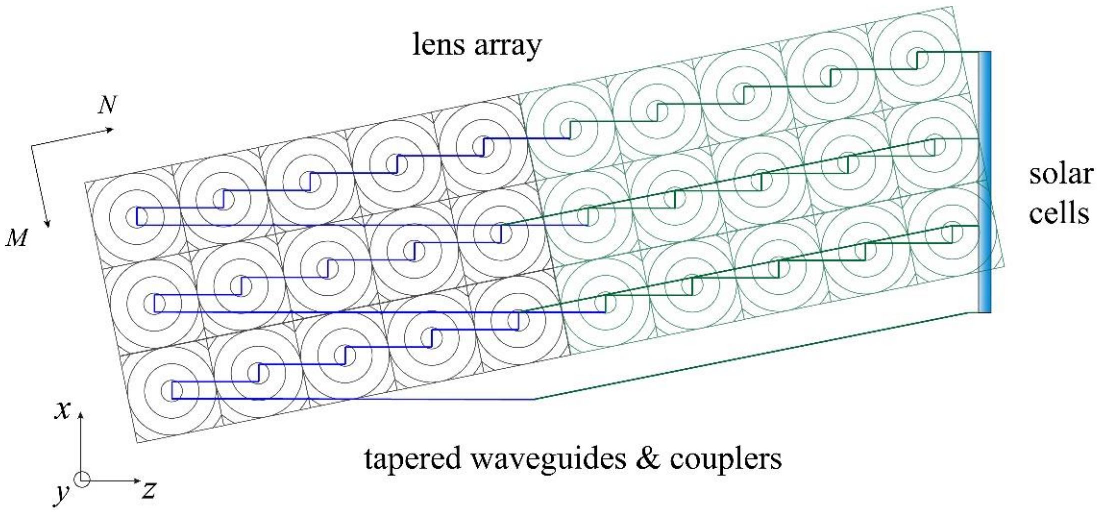

Figure 33. A top view of an integrated tapered waveguide structure. The added waveguides are marked as green.

In order to achieve higher concentration without a separate secondary concentrator, tapered waveguides are used as an integrated part of the primary structure, as illustrated in Figure 33. In this particular example, the ratio D/W is kept the same as a basic structure ($N_0 = 5$), while the number of lenses in a row is doubled. The total concentration therefore increases by $C_W = 2$. This is made possible by tapering the added waveguides to avoid overlapping with the existing waveguides. The tapered angle is set the same as the lens tilting angle $\Theta = \arcsin\left(W/D\right)$ in order to maximize the fill factor. An arbitrary number of lenses can be added in this way and the increased concentration is always $C_W = N / N_0$. It is important to note that any other design parameters remain unchanged as the original design. The only difference is that the propagation angle increases as light travels along the tapered waveguide as in a separate tapered waveguide. Whenever the propagation angle exceeds the critical angles for TIR, light is lost and the efficiency begins to drop. As can be expected, there exists an upper limit for the tapered waveguide length and hence the number of the lenses N and C_W.

IV.2.2 Simulation and discussion

In order to find the relation between the increased concentration ratio C_W and the efficiency η, a math model is built based on Figure 34. Each time a light ray hits the tapered sidewall, its propagation angle in the XZ plane increases by 2Θ. We can thus trace all the rays from different couplers and calculate the total decoupling loss where the propagation angle exceeds the critical angles (decoupling loss). Referring to Figure 34, with propagation angle (where i is the times a light ray interacts with the sidewalls), the horizontal distances traveled by this particular ray are

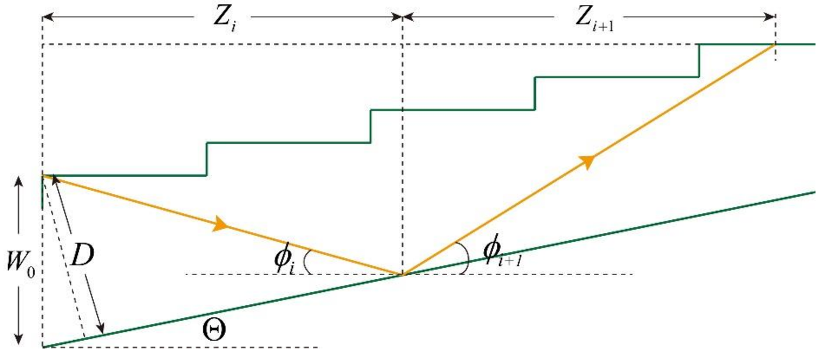

Figure 34. The total propagation efficiency can be estimated by tracing rays from each coupler.

$$Z_i = \frac{D\cos\phi_i}{\sin\left(\phi_i + \Theta\right)}, \text{ and} \tag{IV.4}$$

$$Z_{i+1} = \frac{D\cos\phi_{i+1}}{\sin\left(\phi_{i+1} - \Theta\right)} = \frac{D\cos\left(\phi_i + 2\Theta\right)}{\sin\left(\phi_i + \Theta\right)}, \tag{IV.5}$$

where $\phi_{i+1} = \phi_i + 2\Theta$. Assuming the initial tapering width for all light is $W_0 = \frac{D}{\cos\Theta}$, the maximum concentration achieved without decoupling can be approximated by

$$\begin{aligned} C_{W\max} &= \frac{W_0 + \sum_i Z_i \tan\Theta}{W_0} = 1 + \sum_j \frac{\sin\Theta\left(\cos\phi_j + \cos\phi_{j+1}\right)}{\sin\left(\phi_j + \Theta\right)} \\ &= 1 + \sin 2\Theta \sum_j \cot\left(\phi_j + \Theta\right). \end{aligned} \tag{IV.6}$$

The propagation angle ϕ_i cannot exceed the critical angle $\phi_c = \arcsin\left(1/n_w\right)$. As both of the initial angle ϕ_0 and the lens tilting Θ are determined by lens properties, the waveguide concentration C_W is closely related to the lens array.

As an example, we set the waveguide width $W = 1mm$, the lens focal length $f = 25mm$ and vary the lens diameter D to analyze parameter tradeoffs in this tapered waveguide design. ϕ_0 is estimated using

$$n_W \sin\phi_0 = \sin\left(\arctan\frac{D + w}{2f}\right) \tag{IV.7}$$

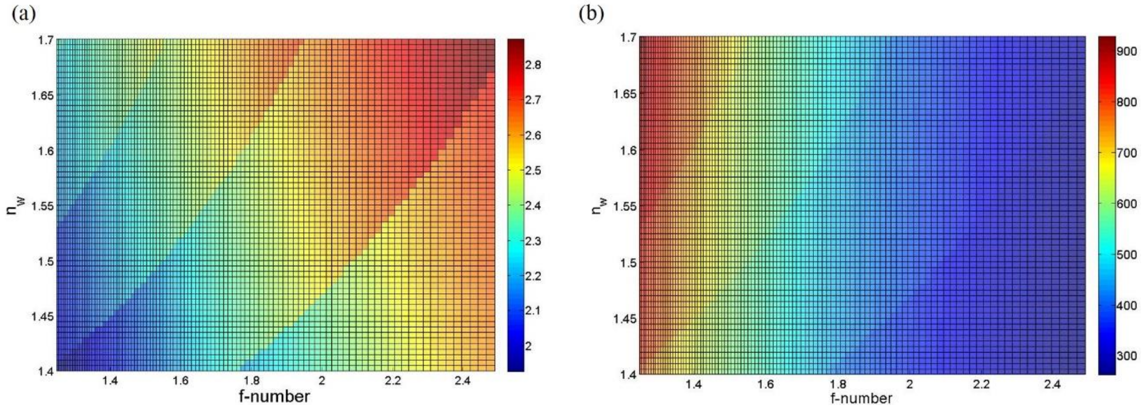

Figure 35. (a) Maximum waveguide concentration C_W as a function of waveguide refractive index n_W and lens f-number. (b) Maximum possible concentration $C = C_W \times C_{lens}$ as a function of n_w and f-number. Both plots consider only decoupling loss in the waveguide as described in Eq. (IV.6).

An index-matching output space is also assumed, as is the case for solar cells. Waveguide concentration C_W and the total concentration $C = C_W \times C_{lens}$ are plotted in Figure 35 respectively as a function of waveguide refractive index n_w and lens f-numbers. The rugged contours indicate interactions between the tapering wall and the light. Small f-numbers have large initial propagation angles ϕ_0 and small lens tilting angles Θ. Light ϕ_0 may interact with the sidewall K times before it exceeds the critical angle ϕ_c, resulting in the discontinuous contours in Figure 35 due to different Ks. Nevertheless, the tapered waveguide structure can boost the concentration up to $C_W = 3$; and under all f-number and waveguide refractive index combinations, a minimum increase of $C_W = 2$ can be expected. As a result, much higher concentration is obtained. Under ideal cases, i.e. no coupling loss between the lens and the coupler, 500~900 geometric concentration can be achieved without any separate secondary optics. Again, we note the plots in Figure 35 assume ideal lens-coupler couplings. Small f-number lenses may bring large aberrations which makes it impossible to focus onto the coupler surface. Under such scenarios, the left part of plots in Figure 35 are not eligible and the total concentration would be limited.

A ZEMAX model is constructed using a Fresnel lens design described previously in IV.1.2. The prism pitch is 200μm and the lens material is PMMA. We select F2 glass as the waveguide material and all the other parameters are kept the same as those in Figure 35. Setting $N_0 = 17$ ($f/1.468$, $C_{lens} = 290$), N is varied to simulate the efficiency at normal incidence, which is illustrated in Figure 36. The efficiency remains at >99% and then begins to drop at $C_W = 2.2$ where light rays exceed critical angle of the waveguide material. Considering the refractive index of F2 at 1750nm is around 1.59, Figure 36 matches well with Eq. (IV.6) plotted in Figure 35(a).

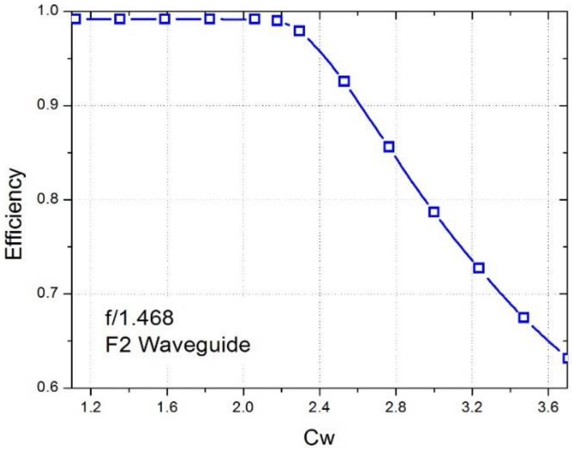

Figure 36. Efficiency plot as a function of waveguide concentration C_W from ZEMAX simulations.

A $C_{geo} = 600$ geometric concentration system is also built based on the results from Figure 36. We use the previous parameters and set $N = 35$ ($C_{lens} = 290, C_W = 2.06$). At normal incidence, it shows 99.5% efficiency where 0.5% light misses the coupler surface. As the structure is asymmetric, its angular response is plotted in a 3D graph in Figure 37. Tilt X and Y represent tracking errors about the X and Y axes defined in the previous figures, where positive angles are clockwise rotations. The acceptance angles (marked as red circle) correspond to 0.5°~0.6° in this structure depending on the tilt orientation. Only structural loss is considered in the above simulations. Fresnel reflections, coupler surface reflection loss and propagation loss are not accounted for.

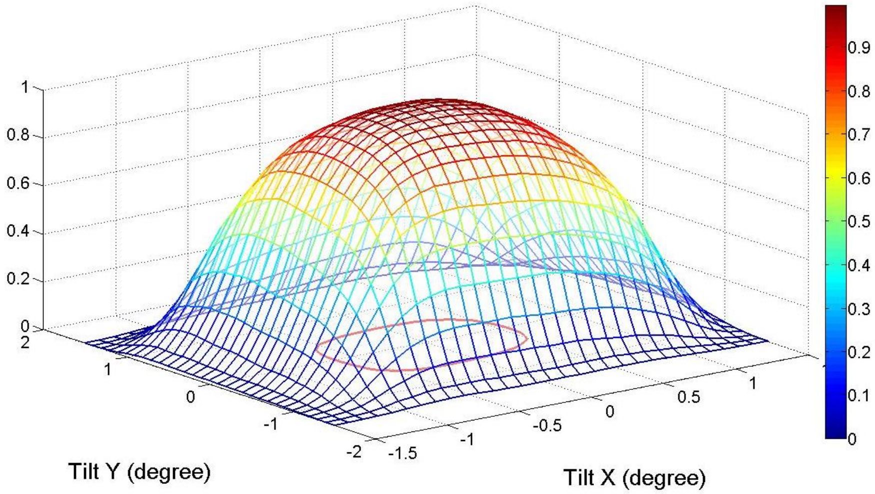

Figure 37. Angular response of a $C_{geo} = 600$ design.

IV.3 A 3D tapered coupler design

IV.3.1 Motivation and introduction

While the integrated tapered waveguide achieves $C_{geo} > 500$ concentration, it is very difficult to approach $C_{geo} = 1000$ concentration (Figure 35). As a result, we extend the concentration in the y-direction, too, in order to further increase concentration.

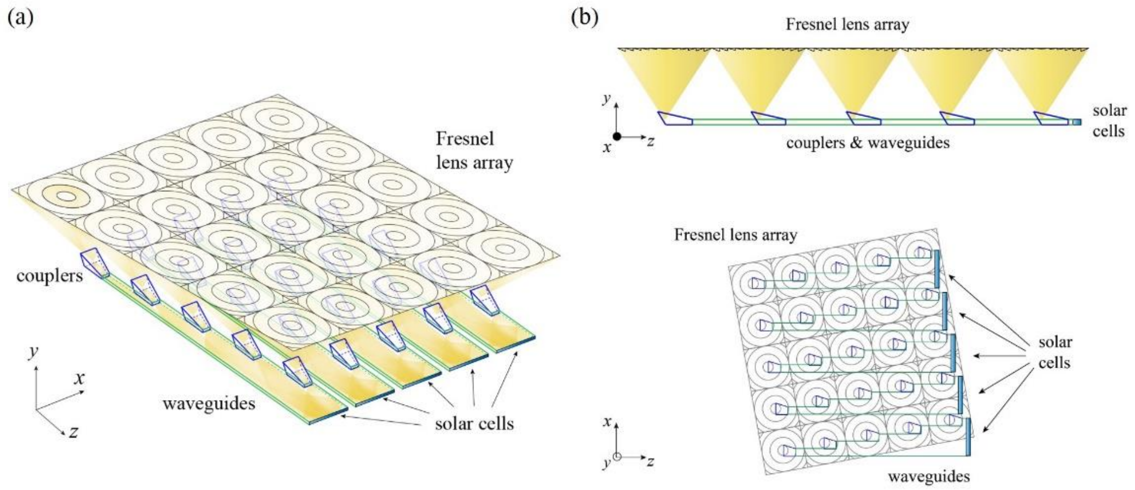

Figure 38. (a) A 3D view and (b) a side/top view of the 3D coupler design.

Figure 38 briefly illustrates the proposed design. Comparing to previous structures, secondary optics are integrated into couplers. These couplers (shown in blue in Figure 38) still has a 45° surface at one end; but a 3D tapering in both x and y directions is added. Such tapering profile provides extra concentration in comparison to tapering in only one dimension, making high concentration (e.g. $C_{geo} = 1000$) achievable. The couplers are designed short and small to make the use of relatively high propagation loss plastic materials possible. Hence these couplers can be economically fabricated, e.g. through molding and pick-and-place process. The waveguides, on the other hand, remain planar and straight. The separation of the coupling and the tapering structures from waveguides may benefit the fabrication process in terms of propagation loss. In all previous designs, both the couplers (i.e. the 45° angled surface) and the tapered structures are parts of the waveguide. It is difficult to pattern the structures into the glass sheet while still remaining transparent, which is a critical issue in the fabrication process. In contrast, the straight wall waveguide can use highly transparent glass materials in this design. Practically, the coupler output and the waveguide input ends are optically connected, e.g. by index-matching gels, to eliminate any possible leakage and to minimize Fresnel reflections. Meanwhile, the sidewalls between the coupler and the waveguides should be optically separated to prevent light in the waveguides propagates into the couplers and decouples from the sidewall, which can be realized by intentionally creating larger separation along the x-axis for each individual coupler to create small air gaps between the side walls.

Assuming geometric concentrations for the lens-coupler pairs and the couplers are C_1 and $C_2 = C_x \times C_y$, respectively, the total structure geometric concentration $C = C_1 \times C_2$. Setting $C = 1000$, different lens properties lead to various possible C_1 and C_2 combinations. Similar to previous structures, the maximum number of lenses along lens axis N is limited by $N < \sqrt{C-1}$ so that waveguides from different rows do not overlap with each other.

The solar cells in Figure 38 are drawn separated from each other as a result of coupler tapering. Whenever desired, the last coupler can be made straight to join solar cells from their neighbors. The decreasing in concentration is essentially small. For example, assuming the last coupler is not tapered in an $N = 30$ design, the total concentration comparing to the initial design is calculated as $C'/C = 30/\left(29+\sqrt{C_2}\right)$, which is approximately 96% under $C_2 = 5$.

IV.3.2 Optical designs

IV.3.2.1 The Fresnel lens array

The Fresnel lens array design described in IV.1.2 is used.

IV.3.2.2 Couplers

Couplers are tapered rectangular volumes placed directly at the focal points from the lens array. With one end angled by 45° to redirect light into the structure, the other end is tapered equally in x and y directions ($x_1 = y_1$, $x_2 = y_2$ and $\sigma_x = \sigma_y = \sigma$ in Figure 39). Secondary concentration is thus provided by $C_2 = \left(x_1/x_2\right)^2$.

Similar to the analysis in III.4, the maximum possible concentration in the x direction is expressed as

$$C_{2x\max} = \prod_{\phi_0}^{90^\circ-\sigma-\phi<\phi_c} \frac{W_i}{W_{i+1}} = \frac{\cos\phi_c}{\sin\left(\phi_0+\sigma\right)}. \tag{IV.8}$$

The same applies to YZ plane as well. Hence the maximum C_2 is approximated by

$$C_{2\max} = C_{x\max}^2 = \left[\frac{\cos\phi_c}{\sin\left(\phi_0+\sigma\right)}\right]^2. \tag{IV.9}$$

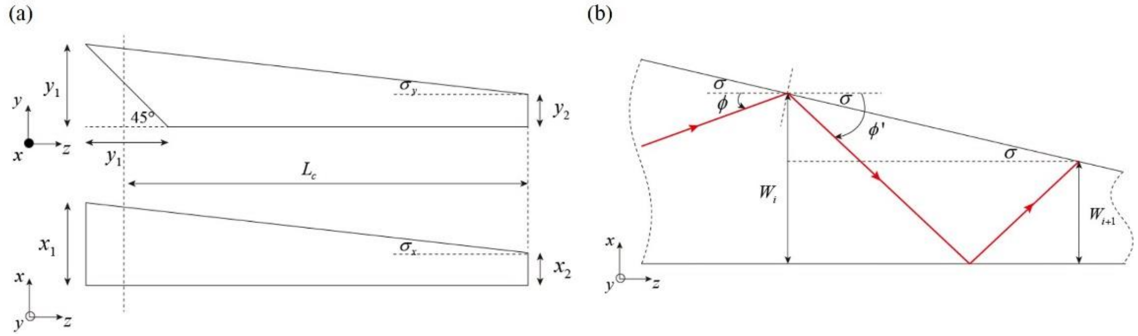

Figure 39. (a) A side view and a top view of the coupler design. The rectangle is equally tapered in both directions. (b) Light propagation in the tapered structure.

ϕ_0 is the initial propagation angle in Eq. (IV.7) and ϕ_c is the waveguide critical angle. Eq. (IV.9) is plotted in Figure 40 as a function of n_w and lens concentration C_1. Higher coupler refractive indices have two major impacts. One is smaller initial angle ϕ_0 and the other is larger critical angle ϕ_c. From an etendue perspective, the output space is consumed by n_w instead of air, leading to n_w^2 increase in the maximum concentration [16]. As ϕ_0 is usually around $10°$, the tapering angle also has noticeable influence on C_2 due to the comparable ϕ_0 and σ in Eq. (IV.9). Large σ tends to flatten the curves, reduce the achievable secondary concentration and shortens the coupler length L_c. The choice of σ will be ultimately determined by the waveguide material selection, where refractive index and absorption coefficient are the most important factors. A $C_{geo} = 1000$ curve is also marked in Figure 40. Any parameter combinations, depending on material availability and practical considerations (e.g. price, manufacturing, stability), can be used to construct the structure as long as they stay above the $C_{geo} = 1000$ line.

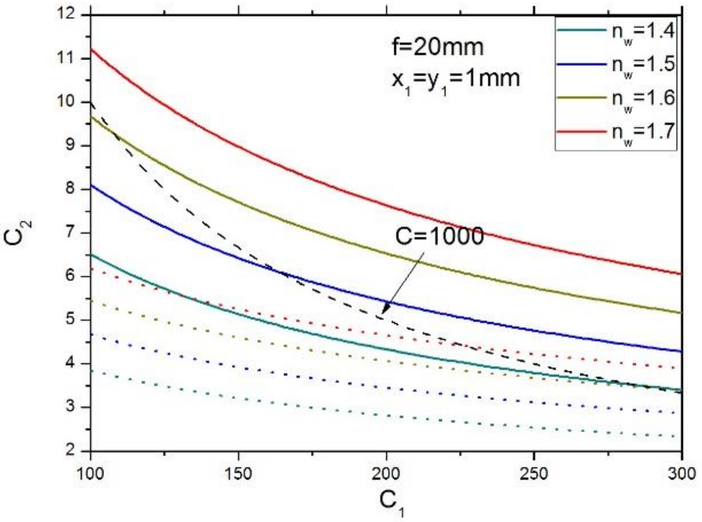

Figure 40. Maximum secondary concentration dependence on primary concentrations. Solid lines and dotted lines assume $\sigma = 5°$ and $\sigma = 10°$, respectively. Black dashed line marks the $C_{geo} = 1000$ curve.

IV.3.2.3 Waveguides

The waveguides are in optical contact with couplers in order to minimize loss on the interfaces. Being the major light guiding component, light travels a long distance inside to reach the output. Waveguide propagation loss stands out as one single important parameter. For example, in an $N = 30$, $D = 14.04mm$ structure, the couplers are always several millimeters while the longest waveguide segment is approximately $L_w = N \times D = 42cm$ (or on average $L_{wavg} \sim 21cm$). A maximum $0.02dB/cm$ average propagation loss is required to get over 90% light transporting efficiency. Again, fabrication process and cost would finally determine the material available for use.

IV.3.3 Simulation and discussion

In order to validate the proposed design method, we construct a $C_{geo} = 1000$ subsystem building block ($M = 1$) in ZEMAX. We use an $N = 30$, $D = 14.04mm$ lens array as the input aperture. Couplers are $1mm \times 1mm$ on the 45° side and $0.4438mm \times 0.4438mm$ on the tapered side. Such combination provides $C_1 = 197$, $C_2 = 5.08$ and a total of $C_{geo} = 1000$ geometric concentration. Couplers and waveguides are PMMA and silica glass, respectively, which are promising candidates for suitable materials. These exemplar parameters are selected as a balance of angular acceptance, material properties and also practical considerations. A detailed list can be found in Table 5.

Table 5. Detailed parameters used for system simulation.

Light Source	**Spectral Range**	**Spectrum**	**Solar Disk**	
	$350nm \sim 1750nm$, $\Delta\lambda = 10nm$	AM 1.5D	$\pm 0.266^\circ$	
Lens Array	**Material**	**Dimensions**	**Individual Lenses**	**Focal Length**
	PMMA	$M = 1$, $N = 30$	$P = 200\mu m$, $D = 14.04mm$	$f = 20mm$
Couplers	**Material**	**45 °Side**	**Tapering Side**	**Length**
	PMMA	$x_1 = 1mm$, $y_1 = 1mm$ 100% reflection	$x_2 = 0.4438mm$, $y_2 = 0.4438mm$	$L_c = 5mm$ ($\sigma = 6.35^\circ$)
Waveguides	**Material**			
	Silica			

An index-matching output space is assumed, i.e. the output medium has the same dispersion curve as silica. Efficiency breakdown for such a structure is shown in Table 6. It is able to deliver >98.9% incident rays to the output aperture of the waveguides. Light propagation in waveguides leaks 0.6% in that silica has relatively smaller refractive index comparing to PMMA; some extreme rays decouple when entering the waveguides from the couplers. We point out that these efficiency numbers consider only structural losses. Fresnel reflection loss, material absorption loss and scattering loss should be separately accounted for in a practical design.

Table 6. Efficiency breakdown.

Elements	**Lens Array**	**Couplers**	**Waveguides**	**Total**
Efficiency	99.9%	99.6%	99.4%	98.9%

Structure angular response (Figure 41) is also simulated by tilting the light source as in Figure 37. The acceptance angle is in the range of 0.5°~0.7° depending on orientations. Comparing to the same lens design in Figure 31, however, the acceptance angle is reduced by 0.1°~0.3°mainly due to the tilted 45° at the coupler surface.

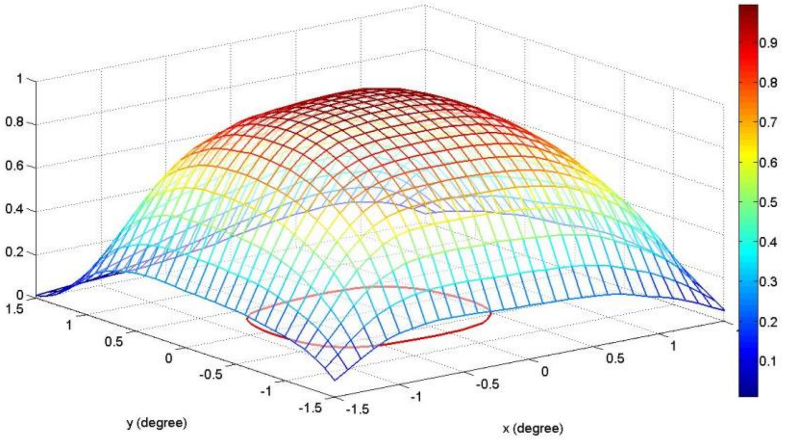

Figure 41. The angular response plot. Red contour line marks 90% efficiency.

CHAPTER V

PRELIMINARY FABRICATION AND MEASUREMENT RESULTS

While the main work presented in this thesis focuses on the design, modeling and simulation of the novel planar lens-waveguide solar concentrator, this chapter briefly documents the preliminary fabrication, prototype building, measurement and testing works in the lab to serve as a memo and guide for future works.

V.1 Waveguide fabrications

V.1.1 Initial fabrications using cleanroom processes

Cleanroom processes (i.e. photolithography) are tested in the first stage of waveguide fabrication work. In order to develop a $45°$ angled structure, we use an inclined-surface photolithography technique using Suss Mask Aligner (MA6). SU-8 2075 from MicroChem is selected as the waveguide material. SU-8 is a popular epoxy-based negative photoresist sensitive to UV light used in microelectromechanical systems (MEMS) with a refractive index around 1.64 [38]. We spin coat $100\mu m$ SU-8 on quartz substrates. Since the critical angle between a SU-8 and air interface is only $37.6°$, it is impossible to fabricate a $45°$ coupler in the air. Therefore, we immerse the whole wafer into deionized water (DI water) and place it onto an angled wafer holder. The DI water serves as an index matching material so that a larger coupler angle can be patterned. Another layer of SU-8 is also placed at the back side of the transparent quartz substrate so that any transmitted UV light can be absorbed, minimizing reflection effects during the UV exposure process (Figure 42 [39]).

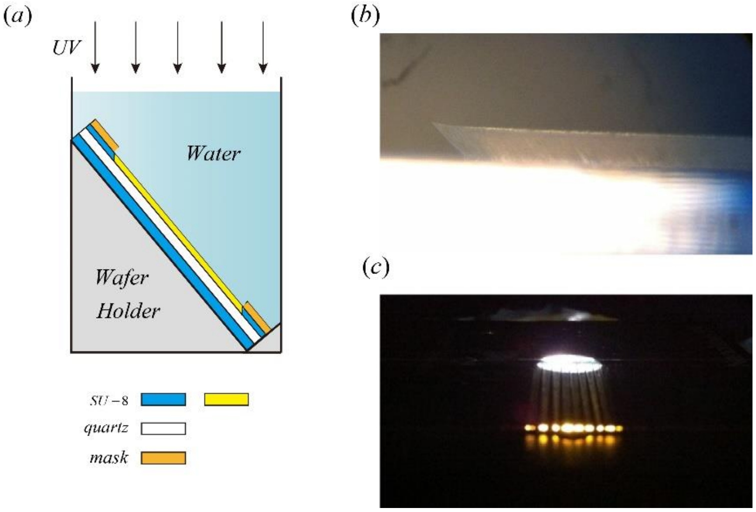

Figure 42. (a) The inclined photolithography setup. (b) Developed 45 degree angled coupler. (c) When a beam of light is focused onto the coupler region, light is coupled through the waveguides [39].

Figure 42 also shows the fabricated device. A 45° coupler is successfully developed (not accurately measured, though). When light is focused onto the couplers, it is guided through the waveguide. The success of using photolithography techniques is limited, though. The main reasons are

- The 45° coupler surface is hard to control;
- It is difficult to find a suitable material that is UV sensitive while transparent enough after curing. It is clear from Figure 42 that SU-8 absorbs short wavelength light and the output appears yellow;
- The thickness of the waveguide is limited to microns and photolithography is not suitable for large-scale fabrications.

V.1.2 CO_2 laser cutter

An alternative method investigated for waveguide fabrication is to use a CO_2 laser cutter cutting acrylic glass sheet. The thickness of the acrylic sheet automatically determines either the x or the y dimension of the waveguide, depending on the cutting orientation (Figure 43). The most straightforward way is to cut the acrylic sheet vertically, defining the 45° angle by the controlling software (x is then the sheet thickness). The drawback is that the waveguides have to be cut piece by piece and placed together instead of as a whole. On the contrary, the laser beam can be tilted by 45° (the power is also reduced). The entire waveguide structure can be cut as a whole in this way. The 45° coupler side, however, is not as accurately controlled as the vertical cut.

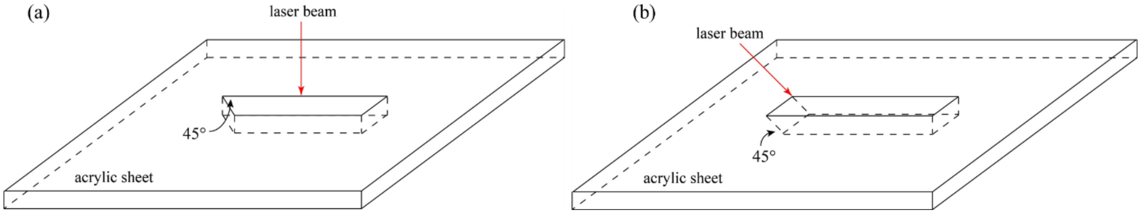

Figure 43. Two different ways of cutting acrylic sheet.

The common issue applies to both cutting orientations is that laser cutting is made possible by melting the acrylic surface and thus the surface quality is not as good, resulting in surface roughness. Although the surface roughness can be minimized by fire polishing [40], currently lots of scattering centers are observed at its surfaces (Figure 44). A more severe problem is that the melt-cut process limits the material selection to plastics which usually are optically inferior to glass. These fabrications issues are part of the reason that we switch to the optimized vertical wall structure mentioned in IV.3.

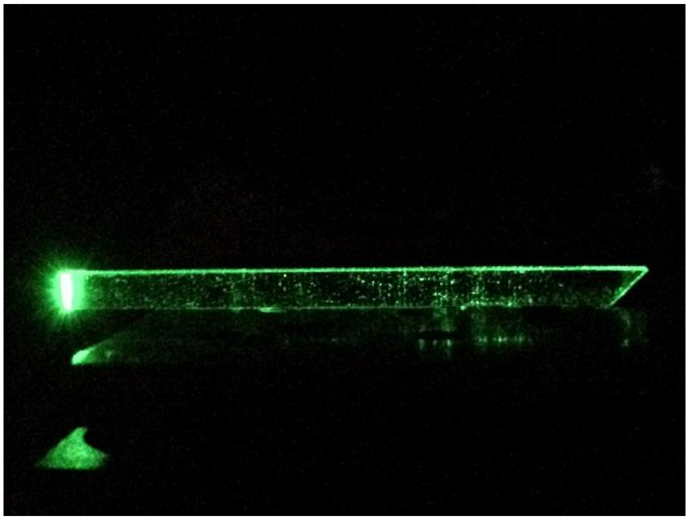

Figure 44. A laser cut waveguide piece illuminated by a green laser beam. Impurities and scattering at the sidewalls are clearly seen.

V.2 Measurement setups

V.2.1 Indoor test setups

An indoor test setup is built to measure prototype performance (Figure 45). A Xenon light source (without filters) is used to roughly mimic the spectrum of sunlight. Two mirrors (mirror 1 and 2, with kinematic mounts, the second mirror faces down towards the optical table while the first mirror is mounted vertically) are used to redirect the light into the device under test (DUT). These mirrors also function as apertures to limit the angular distribution from the light source.

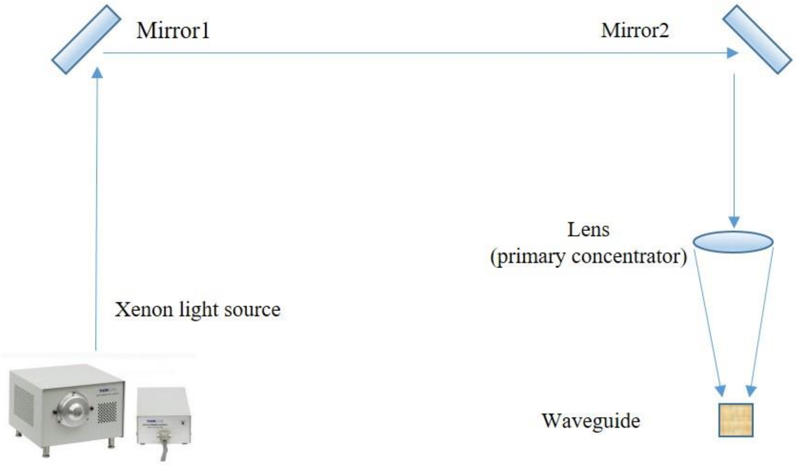

Figure 45. An indoor measurement setup.

When aligning the system, a visible green laser can be used to replace the white light source. Another mirror3 is placed on the optical table and an iris is added between mirror3 and mirror2. The laser beam is tuned by adjusting mirror1 and mirror2 so that it is centered on both sides of the iris. At this point, mirror3 can be removed and a lens is added and adjusted to make sure the laser spot on the table does not deviate after inserting the lens. The waveguide can then be tested. The setup is mainly used to measure single lens-waveguide pairs, including coupler surface quality and propagation loss, and is not suitable for device level measurements due to the limited optics size and accuracy. The setup is also modified to measure oblique angles as described in VI.3.2.

V.2.2 Outdoor test setups

Outdoor testing has the advantage that sunlight is directly available as the light source. To test a system (or a building block), a tracker is needed to make sure the system is aligned with direct normal of the sunlight. A manual tracker is illustrated in Figure 46 using a tripod, which resembles an elevation-azimuth tracker (VI.1.2). The normal direction can be determined by the maximum output of a photodiode or photodetector mounted on the tripod surface. In Figure 46, the waveguide and the lenses are fixed using a 3D printed holder and the holder is fixed at the tracker surface. Note that the concentrated sunlight always exceeds the saturation limit of a detector. Either a neutral density (ND) filter or a III-V photovoltaic cell can be used to uniformly reduce the light intensity or to use photovoltaic short circuit current as an indicator of the optical concentration as shown in Eq. (I.8). In the latter case, the I-V curve needs to be obtained using a source-meter.

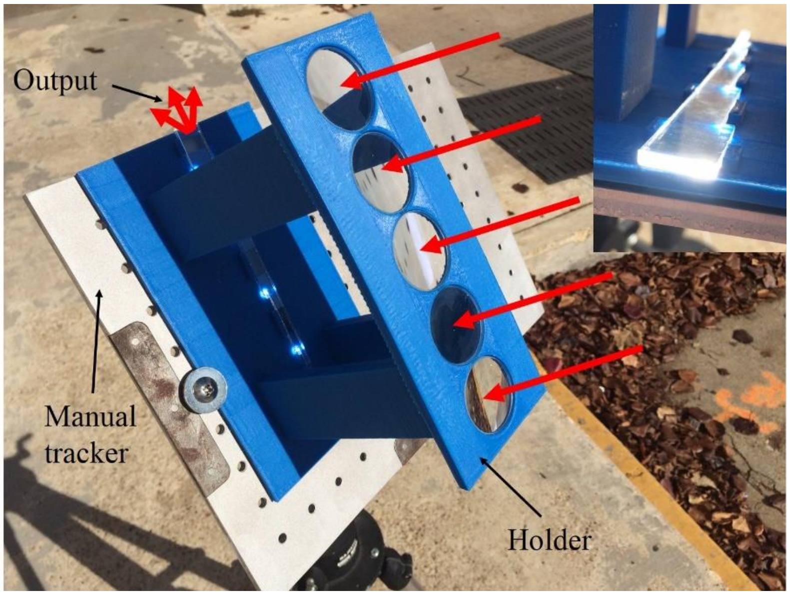

Figure 46. An illustration of the outdoor measurement setup. The whole structure is mounted on a manual tracker. Inset shows the bright output when the lens array is aligned with the Sun.

CHAPTER VI

TRACKING[*]

VI.1 An overview of solar tracking

As CPV optics are designed to take advantage of only direct incident sunlight, solar tracking becomes an integral part in a CPV system to actively point at the Sun all the time throughout the year. High concentration systems usually require precise tracking with accuracy better than 1°. Conventional solar trackers can be divided into two main categories, single-axis and two-axis. While single-axis is mostly used in low concentration systems where the tracking axis is oriented along e.g. East-West or North-South direction, two-axis tracking are commonly used in high concentration systems. This chapter focuses on the discussion of two-axis tracking methods only.

Tracking accuracy depends on a number of factors, e.g. initial installation, sun position equations, open-loop/closed-loop tracking algorithms. This chapter starts with a brief introduction to the Sun movement using equations from [41, 42] and then reviews conventional and novel tracking methods. We are concerned about ideal designs rather than their practical implementations and use relatively simple equations to describe the Sun movement in order to better illustrate tracking methods. A much more complicated and accurate sun position calculation can be found in [43].

---

[*] Part of this chapter is reprinted with permission from "Two-axis tracking using translation stages for a lens-to-channel waveguide solar concentrator," Y. Liu, R. Huang, and C. K. Madsen, *Optics Express*, vol. 22, pp. A1567-A1575, 2014, copyright 2014 by OSA.

VI.1.1 Motion of the Sun

The apparent position of the Sun in the sky varies throughout the day due to the rotation of Earth about its axis. At a fixed location, the angles of the Sun with respect to Earth surface depends on the latitude, longitude, day of the year, and time of day. Latitude and longitude can be determined accurately using global positioning system (GPS). Time of day is always more conveniently represented by local solar time (LST), where 12:00 noon is defined as when the Sun is highest in the sky. LST is usually different from local time (LT) due to time zones, daylight saving adjustments, and the eccentricity of the Earth's orbit. LST and LT can be related by the time correction factor (TC)

$$LST = LT + TC = LT + \left[4\,\mathrm{min}/{}^\circ \times \left(longitude - LSTM \right) + EoT \right]. \qquad \text{(VI.1)}$$

TC is composed by two parts. Error of time (EoT) is an empirical equation that corrects for the eccentricity of the Earth's orbit and the Earth's axial tilt, expressed by,

$$EoT\left(\text{minutes}\right) = 9.87\sin 2B - 7.53\cos B - 1.5\sin B, \qquad \text{(VI.2)}$$

where $B = \frac{360}{365}\left(N - 81\right)$ in degrees and N is the N$^{\text{th}}$ day since the start of the year. The second part of TC, on the other hand, accounts for LST variations in a time zone for different longitudes. The factor of 4 represents 4 minutes for every 1° difference from the local standard time meridian (LSTM).

With the above time definitions, the Sun's position can be described by two angles in the Earth-center frame. Referring to Figure 47, declination angle δ is defined as the angle between the equator plane and a line connecting Earth center and the Sun center, expressed as

$$\delta = \arcsin\left(\sin 23.45^\circ \sin B\right). \tag{VI.3}$$

The other angle is hour angle ω, which indicates the time of day with respect to solar noon,

$$\omega = 15^\circ\left(LST - 12\right). \tag{VI.4}$$

The hour angle is 0° at solar noon and Earth rotates 15° each hour. In the morning the hour angle is negative and it becomes positive in the afternoon. With δ and ω, the Sun position in the Earth center frame is

$$\overrightarrow{EC} = \left(M, E, P\right)' = \begin{pmatrix} \cos\delta\cos\omega \\ -\cos\delta\sin\omega \\ \sin\delta \end{pmatrix} \tag{VI.5}$$

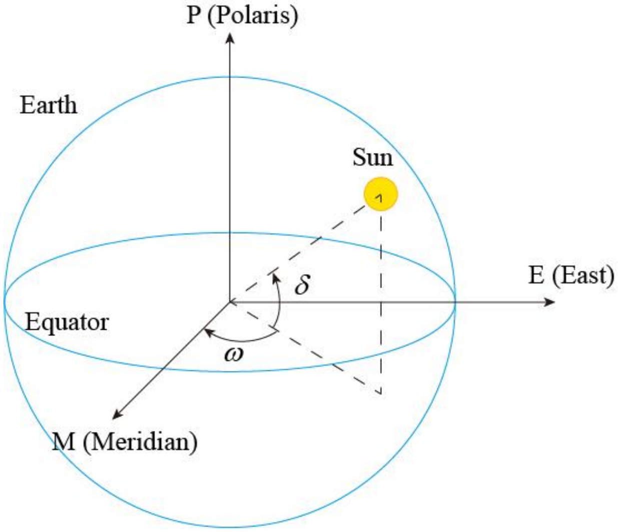

Figure 47. Angle definitions in the Earth centered frame.

A more straightforward coordinate system is the Earth surface frame by rotating the Earth centered frame along East by local latitude φ as in Figure 48. The coordinates in Eq. (VI.5) are multiplied by a rotation matrix to get a new set of coordinates in the Earth surface frame,

$$\overrightarrow{ES} = \left(Z, E, N\right)' = \begin{pmatrix} \cos\varphi & 0 & \sin\varphi \\ 0 & 1 & 0 \\ -\sin\varphi & 0 & \cos\varphi \end{pmatrix} \overrightarrow{EC} = \begin{pmatrix} \cos\varphi\cos\delta\cos\omega + \sin\varphi\sin\delta \\ -\cos\delta\sin\omega \\ -\sin\varphi\cos\delta\cos\omega + \cos\varphi\sin\delta \end{pmatrix}. \qquad \text{(VI.6)}$$

Two frequently used angles in the Earth surface frame are elevation angle α and azimuth angle Azi. Elevation angle is the complimentary angle between the Sun and Zenith, i.e.

$$\alpha = \arcsin\left(\cos\varphi\cos\delta\cos\omega + \sin\varphi\sin\delta\right). \qquad \text{(VI.7)}$$

It indicates how high the Sun is in the sky. On the other hand, azimuth angle is the compass angle that specifies which direction the Sun comes from. Azi is the angle between the local North and the Sun projection on Earth,

$$Azi = \begin{cases} \arccos\left(\dfrac{-\sin\varphi\cos\delta\cos\omega + \cos\varphi\sin\delta}{\cos\alpha}\right), LST < 12 \\ 360° - \arccos\left(\dfrac{-\sin\varphi\cos\delta\cos\omega + \cos\varphi\sin\delta}{\cos\alpha}\right), LST \geq 12 \end{cases}. \qquad \text{(VI.8)}$$

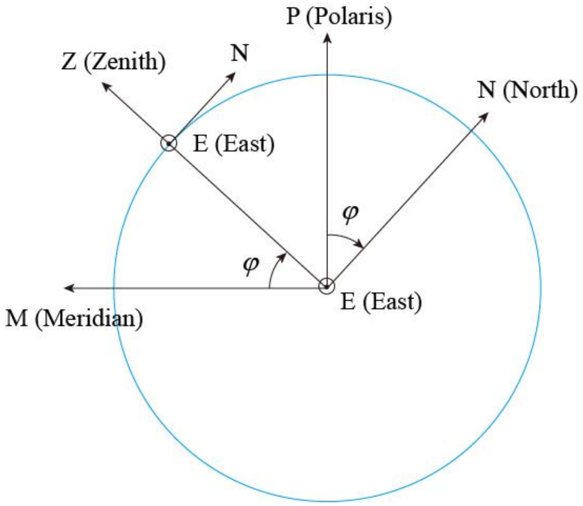

Figure 48. Angle definitions in the Earth surface frame.

A typical elevation-azimuth plot is shown in Figure 49 for College Station, Texas ($\text{longitude}=96.3144°$, $\text{latitude}=30.6014°$) at the 21st day of each month. The Sun is at almost $85°$ elevation on Summer Solstice and at $35°$ on Winter Solstice at solar noon ($LST = 12:00$). The Sun position shifts between the red line and the blue line in Figure 49; sun rise and sun set can also be easily read at $\alpha = 0$ for each curve. Note as the latitude of College Station is larger than $23.45°$, the Sun is always in the southern sky.

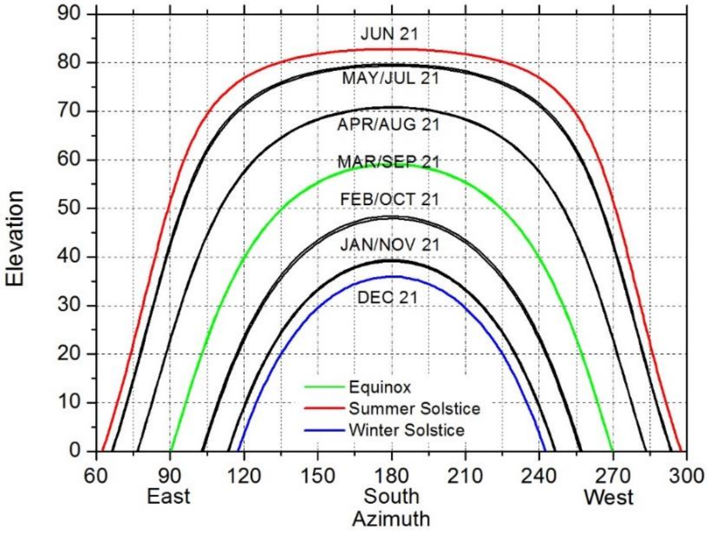

Figure 49. Elevation-azimuth plot for College Station, Texas for the 21st day of each month.

VI.1.2 General formulas for on-axis solar tracking systems

While elevation and azimuth angles are most useful for systems parallel with local Earth surface, a concentrating system sitting on a tracker changes its orientation throughout the day and it is rarely in the same plane with the Earth surface. Hence another collector centered coordinate frame is introduced following the definitions in [44], as illustrated in Figure 50, to describe the Sun movement seen by a solar tracker. OV is defined as vertical axis in parallel with first rotational axis of the tracker; OH and OR forms a plane where the collector surface is driven relative to when it is perpendicular to OV. Angles θ between the surface normal and OV and β between the surface normal projection and OR are angles describing motion of the Sun in such a collector centered frame. They specify rotation speed of the two axes of a perfect tracker. Similar to Eq. (VI.5), the coordinates are calculated by

$$\overrightarrow{CC} = (V, H, R)' = \begin{pmatrix} \cos\theta \\ \sin\theta \sin\beta \\ \sin\theta \cos\beta \end{pmatrix}. \qquad \text{(VI.9)}$$

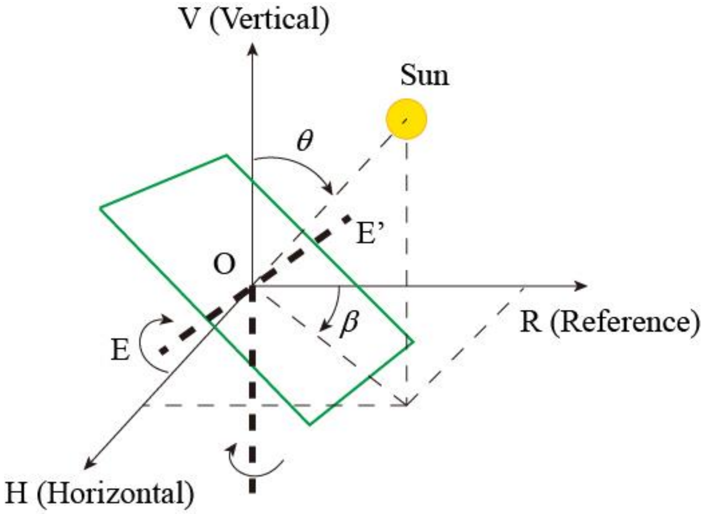

Figure 50. Angle definitions in the collector centered frame.

As a tracker can be orientated in any arbitrary directions, the collector centered frame and the Earth surface frame can be related by three subsequent rotations, i.e. first rotation about Zenith OZ (OV) by ϕ, second rotation about OR' by λ and final rotation about OH by ζ . ϕ, λ and ζ are positive when the rotations are clockwise (Figure 51). Mathematically, these rotations are represented by three rotation matrices,

$$[\phi] = \begin{bmatrix} 1 & 0 & 0 \\ 0 & \cos\phi & -\sin\phi \\ 0 & \sin\phi & \cos\phi \end{bmatrix}, \qquad \text{(VI.10a)}$$

$$[\lambda]=\begin{bmatrix}\cos\lambda & -\sin\lambda & 0\\ \sin\lambda & \cos\lambda & 0\\ 0 & 0 & 1\end{bmatrix}, \tag{VI.10b}$$

$$[\zeta]=\begin{bmatrix}\cos\zeta & 0 & \sin\zeta\\ 0 & 1 & 0\\ -\sin\zeta & 0 & \cos\zeta\end{bmatrix}. \tag{VI.10c}$$

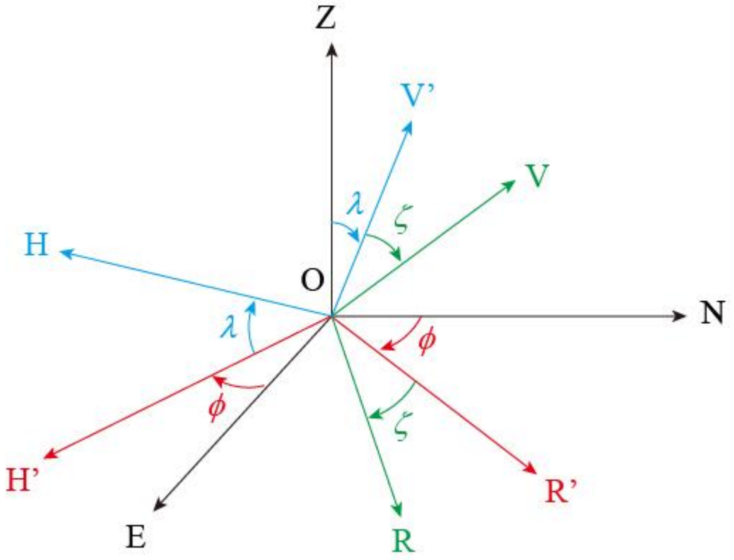

Figure 51. The collector centered frame is formed by rotating the Earth surface frame by three angles.

Combining Eqs. (VI.6), (VI.9) and (VI.10),

$$\overrightarrow{CC}=(V,H,R)'=\begin{pmatrix}\cos\theta\\ \sin\theta\sin\beta\\ \sin\theta\cos\beta\end{pmatrix}=[\zeta][\lambda][\phi]\overrightarrow{ES}. \tag{VI.11}$$

Angles θ and β can be calculated as

$$\theta = \arccos \left[\begin{array}{l} \cos\delta \cos\omega \left(\cos\zeta \cos\lambda \cos\varphi - \cos\zeta \sin\lambda \sin\phi \sin\varphi - \sin\zeta \cos\phi \sin\varphi \right) \\ + \cos\delta \sin\omega \left(\cos\zeta \sin\lambda \cos\phi - \sin\zeta \sin\phi \right) \\ + \sin\delta \left(\cos\zeta \cos\lambda \sin\varphi + \cos\zeta \sin\lambda \sin\phi \cos\varphi + \sin\zeta \cos\phi \cos\varphi \right) \end{array} \right] \tag{VI.12}$$

$$\beta = \begin{cases} \arcsin \dfrac{\left[\begin{array}{l} \cos\delta \cos\omega \left(\sin\lambda \cos\varphi + \cos\lambda \sin\phi \sin\varphi \right) \\ - \cos\delta \sin\omega \cos\lambda \cos\phi \\ + \sin\delta \left(\sin\lambda \sin\varphi - \cos\lambda \sin\phi \cos\varphi \right) \end{array} \right]}{\sin\theta}, \cos\beta \geq 0 \\ 180° - \arcsin \dfrac{\left[\begin{array}{l} \cos\delta \cos\omega \left(\sin\lambda \cos\varphi + \cos\lambda \sin\phi \sin\varphi \right) \\ - \cos\delta \sin\omega \cos\lambda \cos\phi \\ + \sin\delta \left(\sin\lambda \sin\varphi - \cos\lambda \sin\phi \cos\varphi \right) \end{array} \right]}{\sin\theta}, \cos\beta < 0 \end{cases} \tag{VI.13}$$

where $\cos\beta = \dfrac{\left[\begin{array}{l} \cos\delta \cos\omega \left(-\sin\zeta \cos\lambda \cos\varphi + \sin\zeta \sin\lambda \sin\phi \sin\varphi - \cos\zeta \cos\phi \sin\varphi \right) \\ + \cos\delta \sin\omega \left(-\sin\zeta \sin\lambda \cos\phi - \cos\zeta \sin\phi \right) \\ + \sin\delta \left(-\sin\zeta \cos\lambda \sin\varphi - \sin\zeta \sin\lambda \sin\phi \cos\varphi + \cos\zeta \cos\phi \cos\varphi \right) \end{array} \right]}{\sin\theta}$.

Once rotation angles ϕ, λ, and ζ are set, the Sun position in the collector centered frame is derived from Eq. (VI.13). For example, the simplest form of two-axis tracking is an elevation-azimuth collector, where $\phi = \lambda = \zeta = 0$. In this case,

$$\theta = \arccos\left(\cos\delta \cos\omega \cos\varphi + \sin\delta \sin\varphi \right), \text{ and} \tag{VI.14}$$

$$\beta = \begin{cases} \arcsin\left(\dfrac{-\cos\delta \sin\omega}{\sin\theta} \right), \dfrac{\cos\delta \cos\omega \sin\varphi + \sin\delta \cos\varphi}{\sin\theta} \geq 0 \\ 180° - \arcsin\left(\dfrac{-\cos\delta \sin\omega}{\sin\theta} \right), \dfrac{\cos\delta \cos\omega \sin\varphi + \sin\delta \cos\varphi}{\sin\theta} < 0 \end{cases}. \tag{VI.15}$$

θ and β are then the precise two-axis rotating angles in an elevation-azimuth tracker.

Another useful example is polar (tilt-roll) tracking method by setting $\phi = 180°$, $\lambda = 0$, and $\zeta = \varphi - 90°$ (Figure 52). Hence the angles are

$$\theta = 90° - \delta, \text{ and} \tag{VI.16}$$

$$\beta = \omega. \tag{VI.17}$$

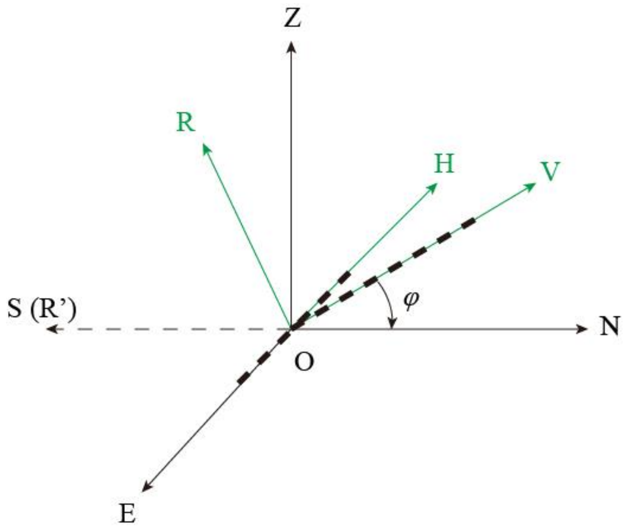

Figure 52. Polar (tilt-roll) tracking.

In a single axis tracker, tracking equations can be obtained by setting either of the tracking angles a constant value. In a latitude-tilted one axis tracker, it follows Eq. (VI.17) $\beta = \omega$ and the other angle is fixed; the system normal is always $\Delta\theta = \delta$ from the Sun. Figure 53 compares available direct normal energy between a two-axis tilt-roll tracker, a latitude tilt one-axis tracker, and a latitude-orientated fixed panel at College Station, where air mass (AM) and direct sunlight energy are calculated using

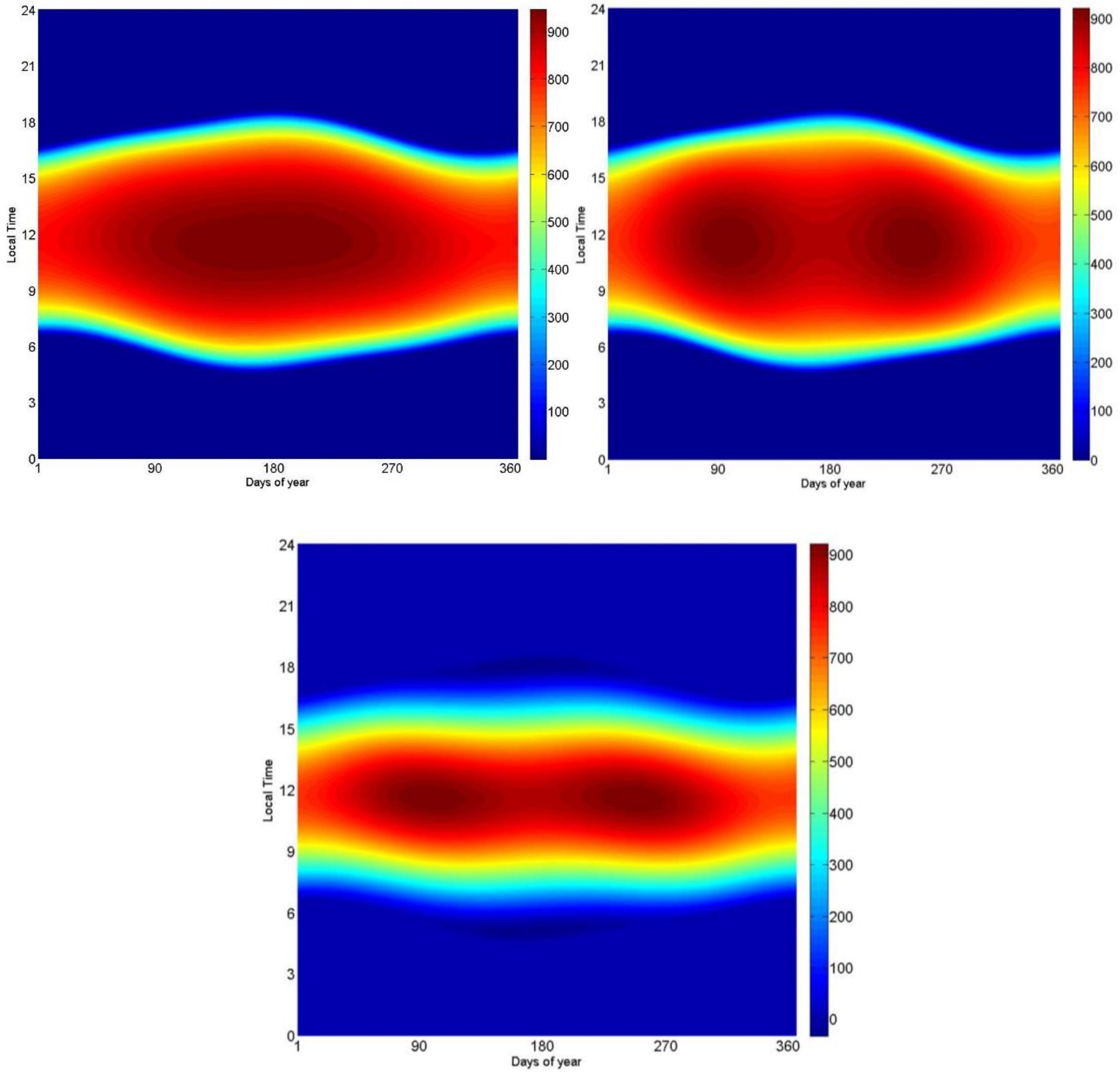

Figure 53. Available solar energy comparison between a two-axis tilt-roll tracker, a latitude tilt one-axis tracker, and a latitude-orientated fixed panel.

$$AM = \frac{1}{\cos\left(90^\circ - \alpha\right) + 0.50572 \times \left(6.07995^\circ + \alpha\right)^{-1.6364}} \text{ [45],} \qquad \text{(VI.18)}$$

$$I_D = 1353 W / m^2 \times 0.7^{AM^{0.678}} \text{ [41].} \qquad \text{(VI.19)}$$

The maximum incoming energy point exists at Summer Solstice for the two-axis tracking where elevation angle is large and AM is small; meanwhile the cosine factor dominates the other two scenarios and local maximum is at Spring/Fall Equinox when system normal is aligned with the Sun.

VI.2 Review of novel tracking designs for planar waveguide concentrators

While compatible with conventional solar trackers as described above (elevation-azimuth, tilt-roll, etc.), several novel tracking structures are also proposed particularly for planar waveguide concentrators to take advantage of the planar floor map and the breakdown of sunlight collecting aperture.

Baker et al. use light induced nonlinear response from reactive particles inside the waveguide to actively change the coupler location [46]. Couplers cover the entire waveguide region and are separated from the waveguide by a low-index layer. Upon receiving focused beam from the lens array, the refractive index of the low-index layer increases locally in a limited range, becoming high-index region which can couple light into the waveguide. Hence an automatic self-alignment mechanism is formed by such reactive coupling material with the use of some other external trackers. However, it requires a minimal change in refractive index of 0.3, which is not easy to realize and the reactive material also needs precise control and complicated configurations. Very limited experimental results are presented and its complexity makes it less useful in real applications.

Similarly, Zagolla et al. report using light generated bubbles as a coupling feature [47, 48]. Instead of refractive index change, a bubble is generated inside the liquid within the waveguide through infrared absorption, which is used as a coupler to reflect light into the waveguide. They achieve around 40% optical efficiency experimentally using laser beam (460nm and 808nm), not even considering system decoupling loss when multiple bubbles exist inside the waveguide as previously discussed in [24]. Moreover, this structure is not compatible with III-V solar cells because the infrared portion of the spectrum is absorbed to generate heat for the bubble and can be only applied to silicon based cells.

Currently Zagolla et al. are working on another way of generating reactive coupling features based on thermal phase change materials (PCMs) [49-52]. A dichroic layer splits the focused light from the lens array into two parts, where short wavelength <750nm is reflected into the waveguide and long wavelength is used for heating up the PCM. Paraffin wax is used as the PCM that undergoes a volume expansion of about 10% when transiting from a solid phase into a liquid phase at $48^\circ C$. The volume expansion is limited in only upward direction and thus couple light into the waveguide. Only 1% efficiency is measured at the current stage [51] and again the infrared portion of the solar spectrum is lost and it cannot be used with III-V multijunction cells.

Another novel tracking method, comparing to reactive self-trackings mentioned above, is using lateral translations to replace rotational tracking. One main issue is Petzval curvature of a single lens from off-axis illuminations (Figure 54). Jared et al. use a second reflective layer to circumvent the problem [53]. They achieve $\eta > 79\%$ (with another 4%~11% shading loss) in a $C_{geo} = 255$ system up to 60° incidence (verified by an off-the-shelf setup), which is enough to cover seasonal change in a latitude-tilted panel.

Halls et al. studied a double-layer lens array architecture for the same purpose of reducing off-axis aberrations [54]. They achieve 75% for an 128x system in simulation and the prototype device behavior matches closely to their simulation result.

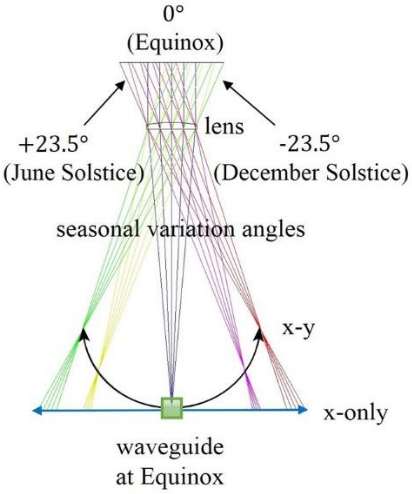

Figure 54. Petzval curvature generated from off-axis illumination. Rays are focused at different focal planes.

VI.3 Two-axis tracking realized by single-axis tracking and a translation stage

VI.3.1 Introduction

As another alternative of using lateral translation instead of rotations, a two-axis tracking scheme designed for $C_{geo} < 250$ concentration realized by a single-axis mechanical tracker and lateral translation is proposed as a possible tracking solution for a planar waveguide concentrator. Lateral translation is used for adjusting positions for seasonal

Sun variation angle δ (Figure 55). With the lens array fixed on the tracker, the waveguide and coupler plane is adjusted both horizontally and vertically (x-y), serving the same purpose of minimizing spot size as described in [53] and [54]. Such method is the easiest and the most straightforward way of reducing field curvature. The lateral translations are associated with single lenses only instead of the whole collection area so that the movement range is small and requires minimum energy.

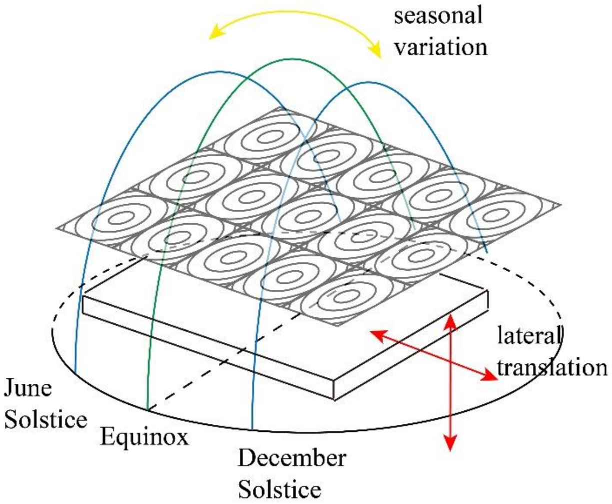

Figure 55. The sky dome seen by a solar system tilted by its latitude. The waveguides is adjusted to accommodate the $\Delta\theta = \delta$ solar seasonal angle variation.

The importance of x-y translations is shown in Figure 56, which compares the spot sizes for x-y to that of horizontal movement. The simulation uses a commercialized aspherical lens from Edmund (#48-172, $D = 23.9mm$, $f/4$) and the incident half angle is increased up to $25°$. The simulation results are calculated by optimizing the full field ($0 \sim 25°$) to give minimum spot size for each field angle. In the horizontal movement case, a V curve is observed because the detector plane is intentionally moved towards the lens to increase the spot size at smaller angles so that the aberrations at larger field angles can be balanced. The spot diagrams in Figure 56(b) clearly shows astigmatism in the x-only scenario and the results are summarized in Table 7.

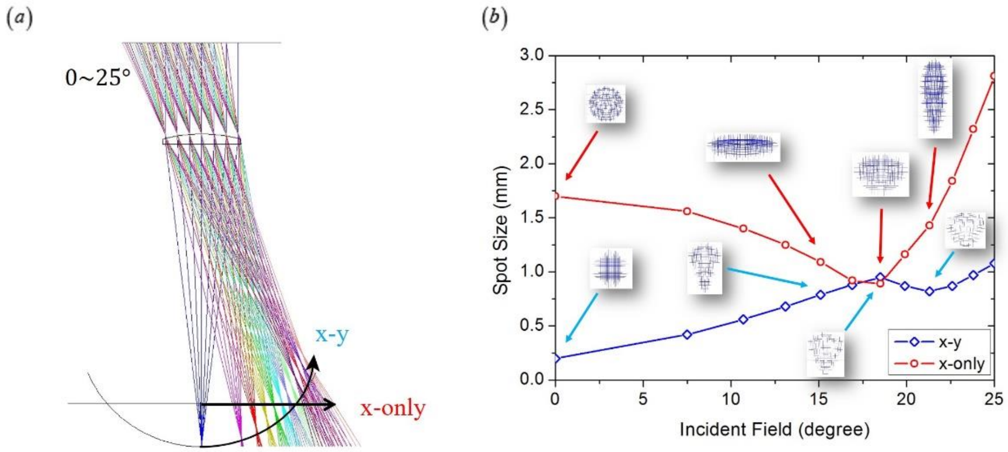

Figure 56. (a) The simulation setup. (b) Spot radius plot using x-only and x-y tuning and the results are summarized in Table 7.

Table 7. Field angles and their corresponding spot sizes.

Fields (°)		0	7.5	10.7	13.1	15.1	16.9	18.5	19.9	21.3	22.6	23.8	25
Spot Size Radius (mm)	x-y	0.20	0.42	0.56	0.68	0.79	0.88	0.95	0.87	0.82	0.87	0.97	1.08
	x only	1.70	1.56	1.40	1.25	1.09	0.92	0.89	1.16	1.43	1.84	2.32	2.81

VI.3.2 Results and discussion

A $C_{geo} = 50$ lens-waveguide prototype is constructed experimentally and simulated in ZEMAX (Figure 57). Again, we use Edmund #48-172 lens and a $3mm \times 3mm$ PMMA waveguide is fabricated using a CO_2 laser cutter ($C_1 = 50$, $C_2 = 1$). In simulation, an ideal blackbody source from 400nm to 1000nm at 5777K with $\pm 0.5^\circ$ incidence angle is used to simulate the Xenon light source in the experimental setup. The refractive index of PMMA, however, is so small that the coupler cannot couple all the light into the waveguide at normal incidence. As the incident angle becomes larger, all incident angles become larger than the critical angle at the coupler surface and the coupling efficiency is in fact increased. Figure 57 shows the simulation results as a function of different incident angles. Although the TIR coupling efficiency at the coupler surface increases up to 100% at higher obliquities, the overall efficiency reaches at its maximum at a certain angle ($\sim 17.5^\circ$ in this setup) and then begins to fall due to the projection factor $\cos\theta$.

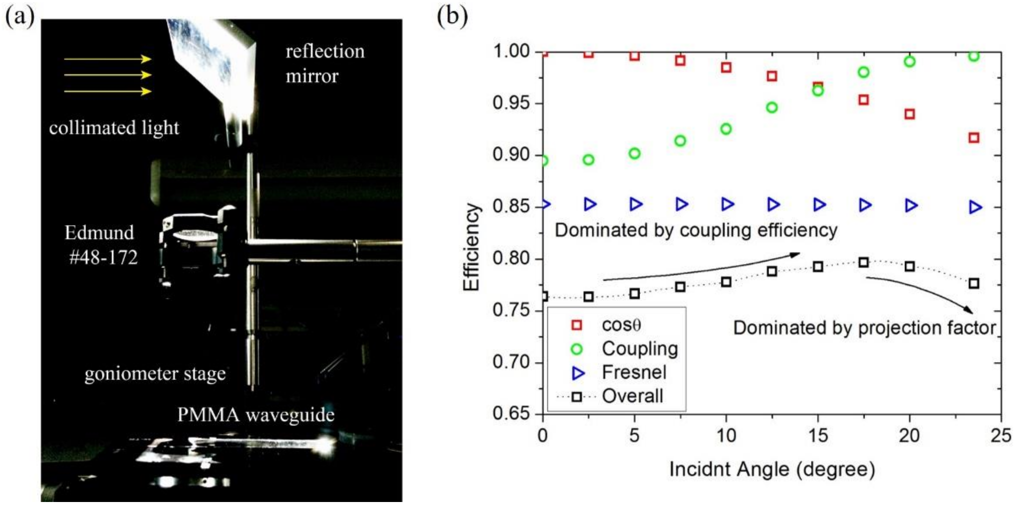

Figure 57. (a) The prototype setup and (b) the plot of the total efficiency $\eta_{overall}$, which is composed of , the TIR coupling efficiency at the coupler surface, the cosine projection factor, and the estimated Fresnel reflection loss .

Experimentally, we mounted the waveguide at the focal point of the lens using the setup described in V.2.1. The angle of the last mirror (mirror2 in Figure 45) in this measurement setup is accurately controlled by a goniometer to simulate different incident angles. The measurement results are plotted in Figure 58 with simulation results. The big difference between x-y and x-only can be easily seen. Note that the required adjustment range for x and y directions are only $34mm$ and $24mm$, respectively, given the parameters used in this setup and they apply to an array structure in the same scale as the array property is totally determined by single lens-waveguide pairs.

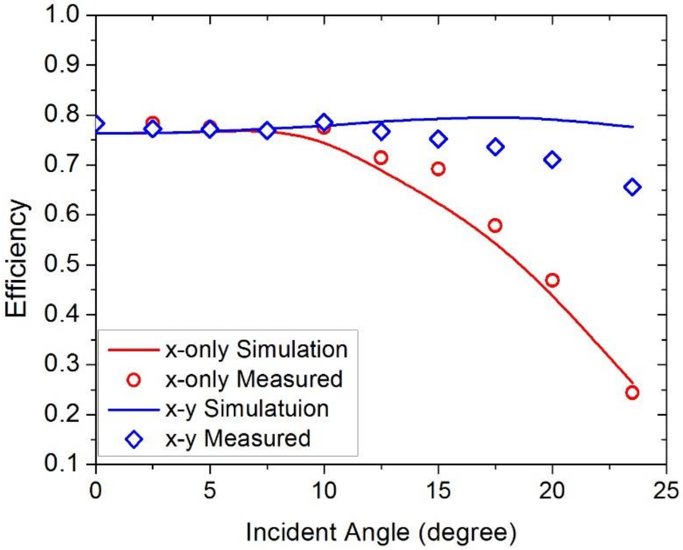

Figure 58. Comparison between simulation and experimental results.

CHAPTER VII

SUMMARY

In this work, a novel planar waveguide solar concentrator is presented. Detailed math models are built and the systems are validated in ray-tracing software ZEMAX. New floor plans are designed as optimizations of the basic structure. Compatible tracking methods are also discussed as an essential part of a solar concentrating system.

Currently the designs have limited success in terms of realization. Prototype lens-waveguide pairs are fabricated using laser cutting techniques. However, the realization of an array structure is not yet achieved, which should be the main goal of current works. The optimized structure in IV.3 makes it possible to separately manufacture the coupler and the waveguide. Several important fabrication factors include

- The roughness of the optical surfaces, including those of lenses, couplers, and waveguides, should be carefully controlled;
- The waveguide material needs to be transparent enough for light traveling inside without reducing efficiency;
- Alignment of the lens and the coupler is accurate.

Indoor measurement setups also need to be refined. A solar simulator might be used to more accurately control the light properties.

The ultimate goal of the system is to work with solar cells. As a result, its integration with III-V multijunction photovoltaic cells may be an important next step. Floor plans of assembling building blocks, spectrum match with cell designs, heat management, and connection issues are all necessary parts of a successful system realization. Furthermore, the reliability and aging issues are also important topics towards the commercialization of the system.

Tracking, as an essential part in outdoor measurements, can be automated using open-loop algorithms described in VI.1.2 or closed-loop feedback circuit or a mix of both. Novel tracking method may also be developed by maximizing the possibility of using lateral translations instead of conventional two-axis rotation trackers.

In conclusion, the proposed planar waveguide solar concentrator shows promising optical performance, validated by both theoretical analysis and simulation results. Works still need to be done towards the successful realization and measurement of the device and integration of III-V multijunction cells.

REFERENCES

[1] S. Shafiee and E. Topal, "When will fossil fuel reserves be diminished?," *Energy Policy,* vol. 37, pp. 181-189, 2009.

[2] V. Smil, *Energy: a beginner's guide*. Oxford, UK: Oneworld, 2006.

[3] S. Hegedus and A. Luque, "Achievements and Challenges of Solar Electricity from Photovoltaics," in *Handbook of Photovoltaic Science and Engineering*, ed Chichester, UK: John Wiley & Sons, Ltd, 2011, pp. 1-38.

[4] J. L. Gray, "The Physics of the Solar Cell," in *Handbook of Photovoltaic Science and Engineering*, ed Chichester, UK: John Wiley & Sons, Ltd, 2011, pp. 82-129.

[5] W. Shockley and H. J. Queisser, "Detailed Balance Limit of Efficiency of p-n Junction Solar Cells," *Journal of Applied Physics,* vol. 32, pp. 510-519, 1961.

[6] A. De Vos and H. Pauwels, "On the thermodynamic limit of photovoltaic energy conversion," *Applied Physics,* vol. 25, pp. 119-125, 1981.

[7] C. H. Henry, "Limiting efficiencies of ideal single and multiple energy gap terrestrial solar cells," *Journal of Applied Physics,* vol. 51, pp. 4494-4500, 1980.

[8] S. P. Philipps, A. W. Bett, K. Horowitz, and S. Kurtz, "Current Status of Concentrator Photovoltaic (CPV) Technology," NREL/TP-6A20-63196, National Renewable Energy Laboratory (NREL), Golden, CO, USA, 2015.

[9] K. Sasaki, T. Agui, K. Nakaido, N. Takahashi, R. Onitsuka, and T. Takamoto, "Development of InGaP/GaAs/InGaAs inverted triple junction concentrator solar cells," *AIP Conference Proceedings,* vol. 1556, pp. 22-25, 2013.

[10] D. Derkacs, R. Jones-Albertus, F. Suarez, and O. Fidaner, "Lattice-matched multijunction solar cells employing a 1 eV GaInNAsSb bottom cell," *Journal of Photonics for Energy,* vol. 2, pp. 021805-1-021805-8, 2012.

[11] V. Sabnis, H. Yuen, and M. Wiemer, "High-efficiency multijunction solar cells employing dilute nitrides," *AIP Conference Proceedings,* vol. 1477, pp. 14-19, 2012.

[12] F. Dimroth, M. Grave, P. Beutel, U. Fiedeler, C. Karcher, T. N. D. Tibbits, *et al.*, "Wafer bonded four-junction GaInP/GaAs//GaInAsP/GaInAs concentrator solar cells with 44.7% efficiency," *Progress in Photovoltaics: Research and Applications,* vol. 22, pp. 277-282, 2014.

[13] R. M. France, J. F. Geisz, I. Garcia, M. A. Steiner, W. E. McMahon, D. J. Friedman, *et al.*, "Quadruple-Junction Inverted Metamorphic Concentrator Devices," *IEEE Journal of Photovoltaics,* vol. 5, pp. 432-437, 2015.

[14] G. Sala, "Concentrator Systems," in *Practical Handbook of Photovoltaics (Second Edition),* ed Boston, MA, USA: Academic Press, 2012, pp. 837-862.

[15] G. Segev, G. Mittelman, and A. Kribus, "Equivalent circuit models for triple-junction concentrator solar cells," *Solar Energy Materials and Solar Cells,* vol. 98, pp. 57-65, 2012.

[16] W. T. Welford and R. Winston, *The optics of nonimaging concentrators: light and solar energy*. New York, NY, USA: Academic Press, 1978.

[17] H. Baig, K. C. Heasman, and T. K. Mallick, "Non-uniform illumination in concentrating solar cells," *Renewable and Sustainable Energy Reviews*, vol. 16, pp. 5890-5909, 2012.

[18] K. Araki and M. Yamaguchi, "Extended distributed model for analysis of non-ideal concentration operation," *Solar Energy Materials and Solar Cells*, vol. 75, pp. 467-473, 2003.

[19] R. Herrero, M. Victoria, C. Domínguez, S. Askins, I. Antón, and G. Sala, "Concentration photovoltaic optical system irradiance distribution measurements and its effect on multi-junction solar cells," *Progress in Photovoltaics: Research and Applications*, vol. 20, pp. 423-430, 2012.

[20] M. Victoria, R. Herrero, C. Domínguez, I. Antón, S. Askins, and G. Sala, "Characterization of the spatial distribution of irradiance and spectrum in concentrating photovoltaic systems and their effect on multi-junction solar cells," *Progress in Photovoltaics: Research and Applications*, vol. 21, pp. 308-318, 2013.

[21] R. Winston, J. C. Miñano, P. Benítez, N. Shatz, and J. C. Bortz, "Nonimaging optical systems," in *Nonimaging Optics*, ed Burlington, MA, USA: Academic Press, 2005, pp. 43-68.

[22] M. Park, K. Oh, J. Kim, H. W. Shin, and B. D. Oh, "A tapered dielectric waveguide solar concentrator for a compound semiconductor photovoltaic cell," *Optics Express*, vol. 18, pp. 1777-1787, 2010.

[23] G. Sala and I. Antón, "Photovoltaic Concentrators," in *Handbook of Photovoltaic Science and Engineering*, ed Chichester, UK: John Wiley & Sons, Ltd, 2011, pp. 402-451.

[24] J. H. Karp, E. J. Tremblay, and J. E. Ford, "Planar micro-optic solar concentrator," *Optics Express,* vol. 18, pp. 1122-1133, 2010.

[25] J. H. Karp, E. J. Tremblay, J. M. Hallas, and J. E. Ford, "Orthogonal and secondary concentration in planar micro-optic solar collectors," *Optics Express,* vol. 19, pp. A673-A685, 2011.

[26] W. C. Shieh and G. D. Su, "Compact Solar Concentrator Designed by Minilens and Slab Waveguide," in *High and Low Concentrator Systems for Solar Electric Applications VI*, San Diego, CA, USA, 2011.

[27] S. Bouchard and S. Thibault, "Planar waveguide concentrator used with a seasonal tracker," *Applied Optics,* vol. 51, pp. 6848-6854, 2012.

[28] S. C. Chu, H. Y. Wu, and H. H. Lin, "Planar lightguide solar concentrator," in *Photonics for Solar Energy Systems IV*, Brussels, Belgium, 2012.

[29] H.-Y. Wu and S.-C. Chu, "Ray-leakage-free sawtooth-shaped planar lightguide solar concentrators," *Optics Express,* vol. 21, pp. 20073-20089, 2013.

[30] K. Arizono, R. Amano, Y. Okuda, and I. Fujieda, "A concentrator photovoltaic system based on branched planar waveguides," in *High and Low Concentrator Systems for Solar Electric Applications VII*, San Diego, CA, USA, 2012, pp. 84680K-84680K-8.

[31] I. Fujieda, K. Arizono, and Y. Okuda, "Design considerations for a concentrator photovoltaic system based on a branched planar waveguide," *Journal of Photonics for Energy,* vol. 2, pp. 021807-021807, 2012.

[32] D. Moore, G. R. Schmidt, and B. Unger, "Concentrated Photovoltaic Stepped Planar Light Guide," in *International Optical Design Conference and Optical Fabrication and Testing*, Jackson Hole, WY, USA, 2010, p. JMB46P.

[33] O. Selimoglu and R. Turan, "Exploration of the horizontally staggered light guides for high concentration CPV applications," *Optics Express,* vol. 20, pp. 19137-19147, 2012.

[34] D. T. Moore, G. R. Schmidt, and B. L. Unger, "Stepped light collection and concentration system, components thereof, and methods," 2010.

[35] M. D. Watson and J. R. R. Jayroe, "Fresnel lens solar concentrator design based on geometric optics and blackbody radiation equation," in *Nonimaging Optics: Maximum Efficiency Light Transfer V*, Denver, CO, USA, 1999, pp. 85-93.

[36] R. Leutz and A. Suzuki, *Nonimaging Fresnel lenses: design and performance of solar concentrators* vol. 83. Verlag Berlin Heidelberg, Germany: Springer, 2001.

[37] A. Davis, "Fresnel lens solar concentrator derivations and simulations," in *Novel Optical Systems Design and Optimization XIV*, San Diego, CA, USA, 2011, pp. 81290J-81290J-15.

[38] MicroChem. (2015). *SU-8 2000 Permanent Epoxy Negative Photoresist Processing Guidelines*. Available: http://www.microchem.com/pdf/SU-82000DataSheet2000_5thru2015Ver4.pdf

[39] Y. Liu, R. Huang, and C. K. Madsen, "A Lens-to-Channel Waveguide Solar Concentrator," in *Renewable Energy and the Environment*, Tucson, AZ, USA, 2013, p. RT3D.1.

[40] Synrad. (2012). *Processing plastics with CO2 lasers, Version 1.03.* Available: http://www.synrad.com/synradinside/pdfs/LaserProcessingGuide_Plastics.pdf

[41] A. B. Meinel and M. P. Meinel, *Applied solar energy: an introduction*. Reading, MA, USA: Addison-Wesley Pub. Co., 1976.

[42] S. Bowden and C. Honsberg. (2015). *PVCDROM*. Available: http://www.pveducation.org/

[43] I. Reda and A. Andreas, "Solar position algorithm for solar radiation applications," *Solar Energy,* vol. 76, pp. 577-589, 2004.

[44] K.-K. Chong and C.-W. Wong, "General Formula for On-Axis Sun-Tracking System," in *Solar Collectors and Panels, Theory and Applications*, ed Rijeka, Croatia: INTECH Open Access Publisher, 2010.

[45] F. Kasten and A. T. Young, "Revised optical air mass tables and approximation formula," *Applied Optics,* vol. 28, pp. 4735-4738, 1989.

[46] K. A. Baker, J. H. Karp, E. J. Tremblay, J. M. Hallas, and J. E. Ford, "Reactive self-tracking solar concentrators: concept, design, and initial materials characterization," *Applied Optics,* vol. 51, pp. 1086-1094, 2012.

[47] V. Zagolla, E. Tremblay, and C. Moser, "Light induced fluidic waveguide coupling," *Optics Express,* vol. 20, pp. A924-A931, 2012.

[48] V. Zagolla, E. Tremblay, and C. Moser, "Efficiency of a micro-bubble reflector based, self-adaptive waveguide solar concentrator," in *Physics, Simulation, and Photonic Engineering of Photovoltaic Devices II*, San Francisco, CA, USA, 2013, pp. 862010-862010-8.

[49] E. J. Tremblay, D. Loterie, and C. Moser, "Thermal phase change actuator for self-tracking solar concentration," *Optics Express,* vol. 20, pp. A964-A976, 2012.

[50] V. Zagolla, D. Dominé, E. Tremblay, and C. Moser, "Self-tracking solar concentrator with an acceptance angle of 32°," *Optics Express,* vol. 22, pp. A1880-A1894, 2014.

[51] V. Zagolla, E. Tremblay, and C. Moser, "Proof of principle demonstration of a self-tracking concentrator," *Optics Express,* vol. 22, pp. A498-A510, 2014.

[52] V. Zagolla, E. Tremblay, and C. Moser, "Demonstration of a 5x5 cm2 self-tracking solar concentrator," in *Physics, Simulation, and Photonic Engineering of Photovoltaic Devices IV*, San Francisco, CA, USA, 2015, pp. 93580G-93580G-6.

[53] J. S. Price, X. Sheng, B. M. Meulblok, J. A. Rogers, and N. C. Giebink, "Wide-angle planar microtracking for quasi-static microcell concentrating photovoltaics," *Nature Communications,* vol. 6, 2015.

[54] J. M. Hallas, K. A. Baker, J. H. Karp, E. J. Tremblay, and J. E. Ford, "Two-axis solar tracking accomplished through small lateral translations," *Applied Optics,* vol. 51, pp. 6117-6124, 2012.